



M a s t e r a r b e i t

Development of accelerator mass spectrometry for ^{93}Zr

Ausgeführt am

Atominstitut

der Technischen Universität Wien

unter der Anleitung von

Univ. Prof. Dipl.-Ing. Dr. techn. Gerald Badurek

durch

Boyana Deneva

Ferdinandstrasse 15/2/15a, 1020, Wien

Datum

Unterschrift (Student)

Abstract

In this master thesis the emphasis was set on the detection of trace amounts of ^{93}Zr as a representative of long-lived fission products ($T_{1/2} = 1.64 \cdot 10^6 \text{ a}$). Because of its trace concentration in many samples, its measurement is a matter of difficulty for most of the detection methods. Only accelerator mass spectrometry can measure ultra low concentrations. The isotopic separation of ^{93}Zr from its stable neighboring isotopes and the isobaric separation from ^{93}Nb have been investigated and optimized.

The measurements were carried out with the Accelerator Mass Spectrometry (AMS) set-up at the Maier-Leibnitz Laboratorium in Garching, Germany. The main experiment was conducted with the Time-of-Flight beam line, using passive absorbers of different thicknesses in form of a stack of silicon nitride foils. Ion beams with high energies, between 80 and 170 MeV were utilized for the measurements. In order to theoretically determine the optimal foil thickness, the simulation program SRIM and numerical calculations with stopping power tables were used. Due to the discrepancies in the results an experimental determination has been performed. This led to optimization of the set-up. The achieved detection limit for ^{93}Zr was $^{93}\text{Zr}/\text{Zr} = 1.7 \cdot 10^{-10}$, presently the lowest value for the detection of ^{93}Zr . The stopping power of the stable ^{92}Zr and ^{94}Zr was also investigated and verified. ^{93}Zr is one example of long-lived fission product, additional measurements with ^{99}Tc were performed. They showed promising results for the implementation of the passive absorber method as a detection technique for ultra trace amounts of a long-lived radioisotope in the mass range around 100 amu.

Additionally, an experimental determination of the separation of ^{93}Nb versus ^{93}Zr by means of a gas filled magnet was made. In order to reduce the isotopic and isobaric background, tests were carried out with different pressure combinations in the magnet chamber and in the detector. Optimizing the conditions led to a detection limit of $^{93}\text{Zr}/\text{Zr} = 4.7 \cdot 10^{-10}$, comparable to the results with the Time-of-Flight beam line.

The results represent the lowest detection limit achieved for ^{93}Zr , without prior chemical processing of the used samples.

1. Introduction

The question of detecting elements with trace level concentration in samples is challenging and complex. The ability to accurately determine isotope ratios of different long-lived isotopes is essential in many fields such as medical treatment, radiometric dating, environmental studies and quality assurance in the nuclear energy sector. The problem with the nuclear waste storage and disposal assessment gives rise to concerns about the long term influence that it might exert on nature and human health. Thus the detection, tracing and monitoring of small amounts of long-lived radionuclides like ^{79}Se , ^{93}Mo , ^{93}Zr and ^{135}Cs has become an essential part of the nuclear fuel (re-) processing as well as disposal.

The determination of trace amounts of radionuclides can provide information about the properties and behavior of the cosmic radiation. The dating of extraterrestrial material is also possible when a time scale in the order of the half-life of the nuclide is considered. Profound studies of the isotopic ratios give valuable insight into the nucleosynthesis models, where the precise determination of different reaction cross sections is of great importance. Back on Earth, the atmospheric transport processes can be monitored by tracking the concentrations of isotopes such as ^{36}Cl and ^{41}Ca . For geological samples the exposition time and erosion rates can be determined by measuring cosmogenic radionuclides, such as ^{10}Be , ^{26}Al or ^{36}Cl .

Due to the low specific activities of all these isotopes, the decay counting methods have limited sensitivity and accurate measurements are cumbersome. An effective way to detect small amounts of long-live radionuclides is to directly count the atoms of the isotope in the sample. This is possible with the Accelerator Mass Spectrometry (AMS), which is a highly sensitive method for determination of the concentration of an isotope of interest in a matrix of stable elements.

This master thesis is oriented to optimisation of the AMS at the Maier-Leibnitz-Laboratory of the Ludwig-Maximilian-Universität and the Technische Universität in Munich, Germany. The aim is the detection of trace amounts of ^{93}Zr .

2. Zirconium

Zirconium is a strong transition metal with atomic number 40, the second element in the Titanium-group, located in group 4 and period 5 of the periodic table. The naturally occurring element consists of five isotopes, four of which stable – ^{90}Zr , ^{91}Zr , ^{92}Zr , ^{94}Zr . The fifth one, ^{96}Zr , is an isotope that is considered stable because of its very long half-life of $2.4 \cdot 10^{19}$ a [1]. From these isotopes ^{90}Zr is the most abundant one with 51.5% of all zirconium.

Zirconium is a common element in the Earth's crust, having concentration around 130 mg/kg [2]. It is not a native element, which means it cannot be found pure in nature. Because of its reactivity it exists bounded in mineral ores and small crystals. The most common sources for the extraction of Zirconium are the minerals Zircon (ZrSiO_4) and Baddeleyite (ZrO_2). Martin Heinrich Klaproth is considered to be the discoverer of this element. In 1789 he analysed the mineral jargon brought from Ceylon, which includes the zirconium-containing mineral zircon, and named the new element Zirconia. It wasn't until 1824 when the Swedish chemist Jöns Berzelius isolated the metal in an impure form for a first time after heating both potassium and potassium-zirconium-fluoride in an iron tube [3].



Figure 2.1. Zirconium crystal bar (Photo: W. Oelen in [4])

Zirconium is solid at room temperature, greyish, lustrous, with good malleability and ductility. This element has a high corrosion resistivity and is considered inert in both its powder and compact metal forms. Nevertheless, it can be dissolved in Hydrofluoric Acid (HF) and Aqua

Regia (mixture of concentrated Hydrochloric Acid and Nitric Acid, ratio 3:1). In powder form it is attacked also by concentrated hot Sulfuric Acid, as well as Phosphoric Acid. Zirconium in metallic form does not oxidise heavily in air at room temperature. However, exposed to Oxygen, even at room temperature, it covers with thin oxide layer, which contributes to the high chemical resistivity of the material. The Zirconium powder should be handled carefully, due to its property to ignite intensely in oxygen-containing atmosphere at temperatures over 180°C [5].

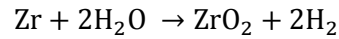
Zirconium finds application in a variety of fields, especially in high temperature and in aggressive environments. Due to its opacity, it is also used in the ceramic industry to confer a white and opaque appearance. This element is a valuable material in vacuum techniques, used as getter in vacuum tubes. Zirconium is used actively also in medicine where it is used in dental implants and restorative treatments, exhibiting biocompatibility and low toxicity [6]. The cubic zirconium in its oxide form has its special place in the jewellery industry as a synthetically produced cheap alternative to the more expensive diamond.

Zirconium alloys are actively used in nuclear technology. They find application in the cladding of nuclear fuel elements and structural components. The fuel elements themselves are made from uranium dioxide powder which is packed in cylindrical pellets. Applying high temperatures, the powder is sintered in order to obtain high density ceramic pellets with nuclear fuel. This method allows the material to have well specified physical properties. The next step is to clad and seal the material in tubes from zirconium alloy. The cladding has the function to prevent fractions from the nuclear fuel to leak out in the coolant and cause contamination. Because of the low thermal neutron absorption cross section of 0.18 b [7], as well as the corrosion resistance, hardness and the good temperature performance, manifested in good thermal conductivity and high melting point, the zircalloys outperform the other common cladding material – steel. There are four types of zircalloys with differing amount of Selenium, Iron, Nickel and Chromium additives, presented in Table 2.1. The most used are zircaloy-2 in Boiling Water Reactors and zircaloy-4 in Pressurized and also Heavy Water Reactors.

Alloy	Mean composition in weight %			
	Sn	Fe	Cr	Ni
Zircaloy-1	2.5	-	-	-
Zircaloy-2	1.5	0.12	0.1	0.05
Zircaloy-3	0.25	0.25	-	-
Zircaloy-4	1.5	0.22	0.1	-

Table 2.1. Composition of zircalloys. Represented from [8].

Among the clear advantages of using zircalloys for nuclear fuel cladding, there is also a very important disadvantage in case of a nuclear accident. If there is a coolant loss, the temperature in the nuclear core rises significantly, which is a precondition for the heavy oxidising of zirconium cladding, following the reaction:



On the example of zircaloy-4 the released energy from this reaction is $\Delta E = 586 \text{ kJ/Mol}$ [9]. Accumulation of the hydrogen in the reactor leads to overpressure and later core explosion because of the formation of oxyhydrogen gas. An example from the near past is the nuclear accident in the Fukushima Daiichi from 2011.

2.1. ^{93}Zr – production and applications

Apart from the already mentioned five stable isotopes of which naturally occurring zirconium consists, there are radioisotopes. A very interesting isotope is ^{93}Zr which has long half-life of $1.64 \cdot 10^6 \pm 0.06 \text{ a}$ [10]. The first evidence for this isotope was delivered from Steinberg and Glendenin in “*A Long-Lived Zirconium Activity in Fission*” from year 1950. They reported a zirconium activity with a half-life in the order of 10^6 a after Uranium irradiation in a pile [11] and related it to Zr isotope with mass 93.

Furthermore, ^{93}Zr is a pure low-energy β^- particle emitter with maximum energy approximately 60 keV [10]. This isotope decays according to the scheme, shown in Figure 2.2.:

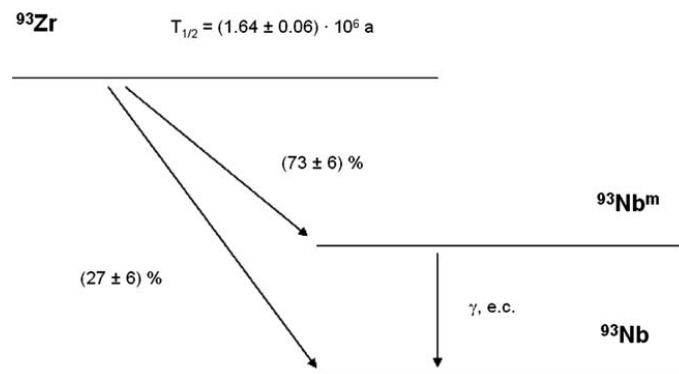
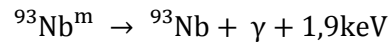
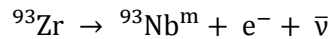
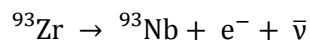


Figure 2.2. Decay scheme of ^{93}Zr . Represented from [10].

On Figure 2.2 are presented the two decay processes. The first one, with a probability of ~73%, is decay to the metastable niveau of $^{93}\text{Nb}^{\text{m}}$ with successive transition to a ground state.



The second one is a direct β^{-} transition to the ground state of ^{93}Nb with decay probability of ~27%:



In the environment ^{93}Zr might be found only in trace amounts, produced by the spontaneous fission of Uranium in Uranium-containing rocks or by neutron activation of ^{92}Zr due to incident atmospheric neutrons. Larger quantities of the isotope can be released from nuclear fallout or by reprocessing plants.

In the next sections a description of different ways of formation of ^{93}Zr is provided.

2.1.1. Nuclear reactors

One way to form ^{93}Zr is as part of the nuclear fuel burning process in nuclear reactors. The common nuclear fuel is usually enriched ^{238}U with ^{235}U and/or ^{239}Pu . ^{235}U is a thermally fissile isotope – fissionable in slow neutron environment such as in light water reactors, which are also the most widespread commercial reactor type. In contrast to ^{235}U , ^{238}U is fissile only for fast neutrons. However, the latter is a fertile isotope, which after a neutron capture and two β decays produces the thermally fissile ^{239}Pu . Figure 2.3 shows the cumulative fission product yields for ^{235}U and ^{239}Pu , where the bimodal mass distribution can be clearly seen. The data is obtained for thermal neutrons.

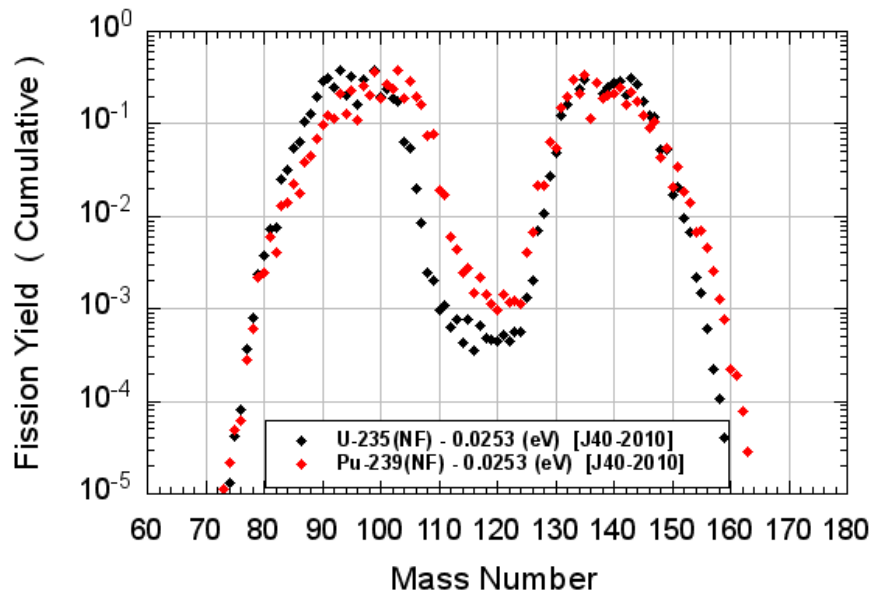


Figure 2.3. Distribution of Fission Products for ^{235}U and ^{239}Pu . Represented from [12]

The fission yield for ^{93}Zr is 6,3% and 3,8% from ^{235}U and ^{239}Pu respectively [12]. Using these yields and conducting a simple calculation the amount of ^{93}Zr in the used nuclear fuel can be obtained. A nuclear fuel with mass 1 kg is considered, consisting of 65% ^{238}U , enriched with 4% ^{235}U , and 35% ^{239}Pu [13]. The neutron flux in the reactor is selected to be $1 \cdot 10^{13} \text{ n/cm}^2\text{s}$ [14] and the irradiation time of the fuel material – 3 years. Considering UO_2 and PuO_2 densities of 10 g/cm^3 and 11.4 g/cm^3 respectively [15] and taking into account the corresponding thermal neutron absorption cross sections for ^{235}U , ^{238}U , ^{239}Pu [16] it is obtained an approximate value of 0.38 g for the ^{93}Zr content in 1 kg spent nuclear fuel. The self-shielding of the fuel, represented in lower neutron flux in the inner than in the outer layers of the nuclear material, was neglected. Despite this relative small percentual amount of ^{93}Zr in the nuclear waste, its very long half life makes it one of the most important isotopes considering spent nuclear fuel storage and disposal assessment. This is also presented on Figure 2.4 where the long-term contribution of ^{93}Zr to the radioactive waste can be seen.

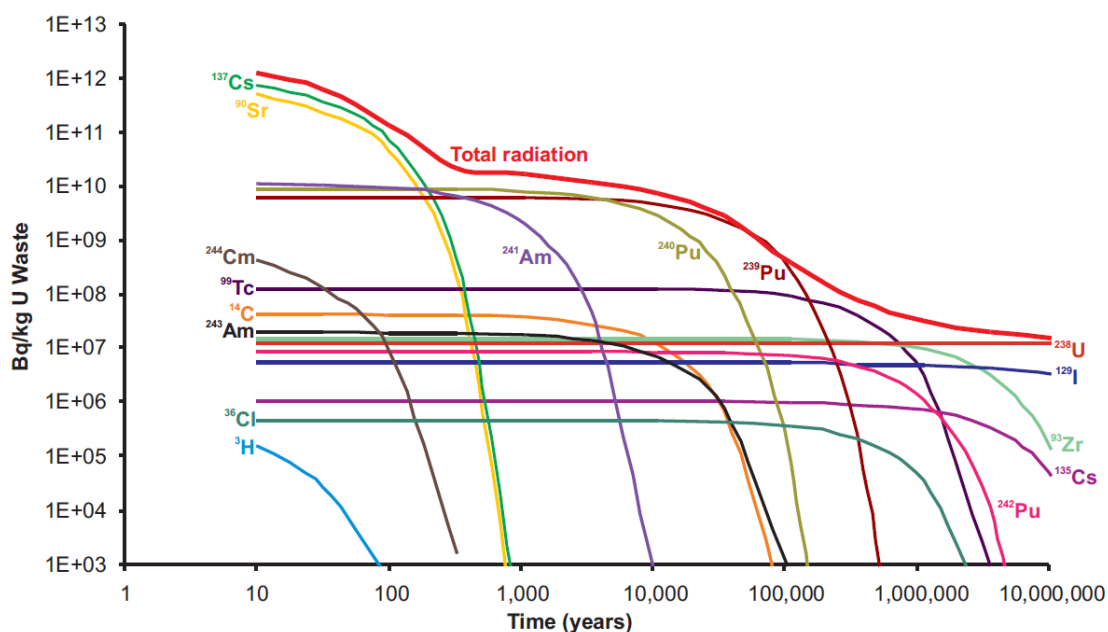


Figure 2.4. Relative activity and decay scheme in high level nuclear waste. ^{93}Zr is presented with light green colour. Represented from [17].

Another way to obtain ^{93}Zr in a nuclear reactor is by neutron activation of ^{92}Zr in the zircaloy cladding of the nuclear fuel elements. The stable isotope ^{92}Zr has very low thermal neutron capture cross section of 0.25 b [18] considering the reaction $^{92}\text{Zr}(n,\gamma)^{93}\text{Zr}$. As a comparison reference, the thermal neutron capture cross section of ^{235}U is 504 b [16], which shows that the rate of production of ^{93}Zr in the nuclear cladding is quite small compared to the one from the nuclear fall-out. However, due to the large amounts of zirconium used in the nuclear vessel components, this type of ^{93}Zr production should also be taken into account when considering accidents in reprocessing facilities or power plants.

The released long-lived radioisotopes from European nuclear reprocessing plants can be used as tracers for mapping and measuring the changes of the ocean currents [19]. This is the case with the reprocessing plants La Hague (France) and Sellafield (Great Britain), which have well known emission rates. Suitable tracer candidates are ^{99}Tc and ^{93}Zr as the ratio of $^{99}\text{Tc} / ^{93}\text{Zr}$ is being determined. Due to the very long half-life of these nuclides there is a small chance of signal loss caused by radioactive decay and they can be traced for a couple of decades. Additionally, the natural amount of ^{99}Tc and ^{93}Zr in the seawater is negligible, which contributes to the accuracy of the measurement. While for a reliable measurement with conventional methods (decay counting) large amounts of water are needed, accelerator mass spectrometry allows a significant reduction of the water samples. That is why a high sensitivity AMS method has to be introduced to detect very small concentrations of the ^{99}Tc and ^{93}Zr isotopes [20].

Additionally, an innovative application of zirconium in nuclear reactors in the form of zirconium dosimeters is being developed by... (France... to add). Applying a dosimeter with known quantity of ^{92}Zr in the reactor vessel and measuring the amount of ^{93}Zr after certain irradiation time could provide information about the neutron flux in the measurement point.

2.1.2. Natural processes

^{93}Zr can be produced also in nature. In the frame of this work ^{93}Zr has been considered for the first time for dating of geological processes.

The first way is through spontaneous fission of Uranium in Uranium-containing rocks. A simple calculation can provide an approximate amount of ^{93}Zr in a chosen rock type. Uranium occurs in different geological environments. For the current consideration a granite rock was considered as an example of the intrusive deposits, being one of the most common representatives of the felsic intrusive igneous rocks. The uranium content was taken to be 2.5 ppm [21], which presents the average content in the upper crust. In order to make a comparison with the nuclear fuel production, 1 kg of granite was considered. The naturally occurring ^{235}U represents only 0.7 % of the whole natural uranium. This makes its contribution to the calculation very low, compared to the contribution of ^{238}U , having natural abundance of 99.28%.

Firstly, the induced fission after thermal neutron absorption was taken into account. If this production process is examined then a neutron source is needed. Atmospheric neutrons have their origin in the interaction of the cosmic rays with the atmosphere due to spallation and evaporation processes of oxygen and nitrogen nuclei [22]. In the calculation are not considered solar neutrons, which have the kinetic energy to reach the ground without decaying only during strong solar storms. The neutron flux on the Earth's surface is approximately $2.5 \cdot 10^{-3}$ neutrons/cm²s, taking into account only the thermal part of the energy spectrum [23] [24]. The natural neutron background in the soil has a small contribution and the total neutron flux results in $3.5 \cdot 10^{-3}$ neutrons/cm²s [25] [26]. The thermal neutron absorption cross section is 504 b as already described above. In order to be able to detect the isotope of interest, the number of ^{93}Zr atoms $N(^{93}\text{Zr})$ and the ratio $^{93}\text{Zr}/\text{Zr}$ is considered. The current accelerator mass spectrometry technique allows detection for $N(^{93}\text{Zr}) > 10^8$ atoms and $^{93}\text{Zr}/\text{Zr} > 10^{-9}$. The implementation of the neutron flux value into the calculation and applying the fission yield for ^{93}Zr of 6.34% results in $6.7 \cdot 10^5$ atoms ^{93}Zr . This value is under the given value for $N(^{93}\text{Zr})$. That is why the detection of this isotope in this rock type can be currently considered a challenge.

The isotope ^{238}U , opposed to ^{235}U , undergoes spontaneous fission to ^{93}Zr with 6.23% production yield. Additionally, the fission probability per decay, ε_{fis} , is in the order of 10^{-7} ,

calculated from the β - and fission decay half-lives [27]. As the daughter isotope ^{93}Zr has much shorter half-life than the mother radionuclide, considering the spontaneous fission, a secular radioactive equilibrium was applied (Equation (2.1)), which occurs after approximately seven half-lives of ^{93}Zr – $11.4 \cdot 10^6$ a. This time interval was also accepted for total interaction time.

$$\frac{dN_{93\text{Zr}}}{dt} = N_{238\text{U}} \cdot \lambda_U \cdot \varepsilon_{fis} \cdot \varepsilon_{93\text{Zr}} - N_{93\text{Zr}} \cdot \lambda_{\text{Zr}} \quad (2.1)$$

The production rate of ^{93}Zr is obtained from the number of ^{238}U atoms in the sample weighted with the corresponding decay constant λ_U and the fission probability per decay ε_{fis} and ^{93}Zr fission yield $\varepsilon_{93\text{Zr}} = 6.23 \cdot 10^{-2}$ [12]. The calculation gives $N(^{93}\text{Zr}) = 1.3 \cdot 10^9$ particles ^{93}Zr , resulting from the spontaneous fission of ^{238}U in granite. According to the considerations above, this is a measurable value. But it is also important if the ratio $^{93}\text{Zr}/\text{Zr}$ will give satisfactory results. The result of $4.7 \cdot 10^{-13}$ is still under the detection limit of 10^{-9} [20].

^{93}Zr can be naturally produced also through neutron activation of the stable ^{92}Zr . As we want to compare both production methods in nature, the same time interval as in the previous calculation of $11.4 \cdot 10^6$ a was considered for the same granite mass of 1 kg. The thermal neutron capture cross section of ^{92}Zr is 0.25 b [18] and the average concentration of zirconium in granite is 400 ppm. This results in $2.7 \cdot 10^7$ particles ^{93}Zr , corresponding to $^{93}\text{Zr}/\text{Zr}$ concentration of $9.6 \cdot 10^{-15}$. The result is challenging for the current detection limits.

The contributions from the induced fission after fast neutron absorption of ^{238}U and the spontaneous fission of ^{235}U to ^{93}Zr are not presented here, due to the small contribution to the overall concentration of ^{93}Zr .

From the conducted calculation can be drawn the conclusion that the spontaneous fission of ^{238}U delivers the highest amount of ^{93}Zr atoms in granite. The concentration is still under the current possibilities. Lowering the detection limit is one of the goals of this thesis and would allow the use of ^{93}Zr for dating with shorter time scale than the usual uranium-lead method – 1 to $4.5 \cdot 10^6$ a.

2.1.3. Nucleosynthesis

The lightest elements H, He, Li were synthesized during the Big Bang. All other heavier nuclei are produced in stars as part of their life cycle. The stellar nucleosynthesis can be divided into two key processes. Elements up to the Iron-group (Fe, Ni, Co) are synthesized in stellar fusion. Most of the heavier than ^{56}Fe nuclei cannot be produced through thermonuclear reactions but are result of neutron capture processes. Neutron capture nucleosynthesis consists of two different processes: s- (slow) process and r- (rapid) process. This notation originates from the timescales needed for the neutron addition compared to the time

needed for the β -decay of the target nuclides. Additionally, the s-process is characterised with low neutron densities in the order of $10^6 - 10^7 \text{ n/cm}^3$ and follows the valley of nuclear stability, while the r-process needs high neutron densities larger than 10^{20} n/cm^3 and produces very neutron rich nuclei. ^{93}Zr has very long half-life, which can be compared to the timescales needed for the s-process. It lies on the main s-process path where after a neutron capture ^{94}Zr is formed, as well as builds one of its branching points via β -decay and formation of ^{93}Nb [28]. This is presented on Figure 2.5.

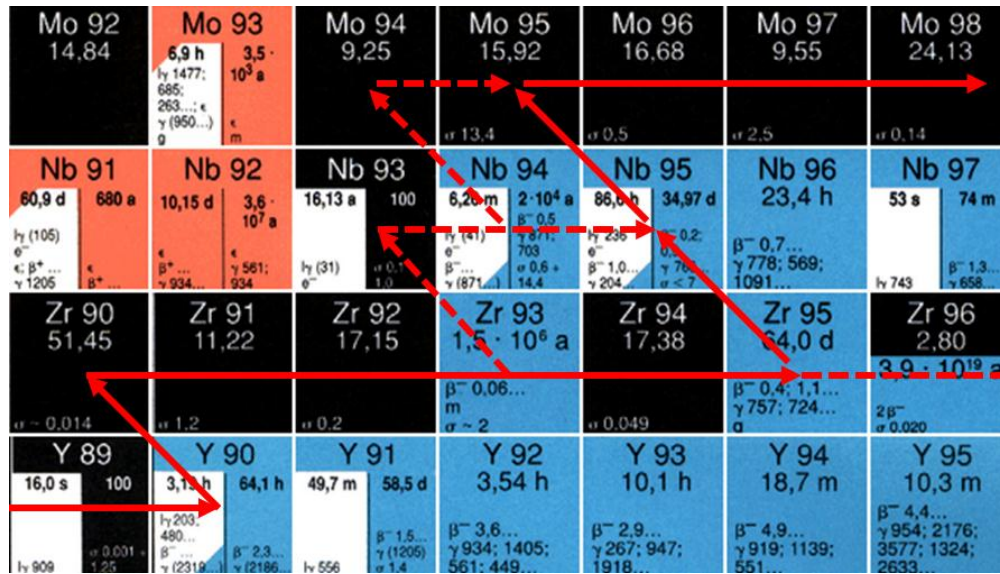


Figure 2.5. S-process for zirconium (bold red line) and the branching at ^{93}Zr (dashed red line). Source [29], modified

The element Zirconium is an essential part in the production of s-process heavy elements. Still, in the literature there is no defined $^{92}\text{Zr}(n,\gamma)^{93}\text{Zr}$ cross section for the temperatures relevant for the s-process [28]. Thus, the study of ^{93}Zr can give an important insight and contribute to the accuracy of stellar models

3. Technical realisation

In the previous sections the importance of isotopic studies in different industrial and scientific fields was pointed out. Especially challenging is the detection of isotopes on trace level in samples. That is why an overview of the most common detection methods and their advantages will be presented in the next paragraphs.

3.1 Overview

Talking about analysis in the isotopic studies, there are two basic detection methods usually used – decay counting and mass spectrometry. For utilizing a method the characteristics of the considered sample of interest should be taken into account.

Decay counting can be used for detecting radionuclides with relatively short half-life. This method includes counting of the isotope decays during the measurement time and determining the decay rate. By knowing this rate, the abundance of the isotope can be either directly determined or through comparison to already known decay rates. The sensitivity of the decay counting method is limited by the concentration of the radioisotope of interest. Without additional equipment for low-level background detection [30], very long measurement sessions or very big samples are needed. Important isotopes, which present difficulties for the common decay counting, are ^{36}Cl and ^{129}I , used for water and ice dating, or fission products, emitted after the nuclear accidents in trace amounts in soil and water. Radionuclides with half-lives longer than a couple of years are particularly difficult to measure. In the example of ^{93}Zr the measurement with decay counting is not possible owing to its trace concentration in the samples and very low activity due to its half-life of 10^6 a. Additionally, there are no certified standards for the measurements of this isotope [31].

The decay counting fails to detect isotopes with very long half-lives. Instead of waiting for the nuclei to decay it is more advantageous to directly count the number of the atoms of interest, where the mass spectroscopy detection methods are successfully utilized. They ionise the sample material and force different isotopes on different trajectories using ion optics. This is a very effective method in obtaining the ratio of the isotope of interest to a known isotope.

One common representative of mass spectrometers for elemental determinations is the Inductively Coupled Plasma Mass Spectrometry or ICP-MS where an inductively coupled plasma source is combined with a mass spectrometer. It can measure the abundance of a specified isotope of an element with high precision. A difficulty presents the isobaric and molecular background of some ions of interest. In Table 3.1 some isotopes are presented with their background. The common ICP-MS technique uses a quadrupole mass spectrometer, which has a sensitivity between 0.7 and 1 atomic mass units [32]. From the mass difference column of Table 3.1 can be seen that with such mass resolution this isobars cannot be separately detected. The high resolution ICP-MS could solve some but not all detection difficulties and in most of the cases additional chemical separation should be performed. For the example of ^{93}Zr to ^{93}Nb , the detection limit for ^{93}Zr is set to a concentration of 50 $\mu\text{g/g}$ or $^{93}\text{Zr}/\text{Zr} = 10^{-6}$ even after chemical separation [33].

Isotope of interest	Interference	$ \Delta m $
$^{52}\text{Cr} = 52.94065$	$^{37}\text{Cl}^{16}\text{O} = 52.96081$	0.02016
$^{56}\text{Fe} = 55.93494$	$^{40}\text{Ar}^{16}\text{O} = 55.95729$	0.02235
$^{40}\text{Ca} = 39.96259$	$^{40}\text{Ar} = 39.96238$	0.00021
$^{87}\text{Sr} = 86.90889$	$^{87}\text{Rb} = 86.90918$	0.00029
$^{93}\text{Zr} = 92.906476$	$^{93}\text{Nb} = 92.90638$	0.00010

Table 3.1. Mass of some isotopes with their molecular/isobaric background in [u]. The mass difference is also calculated. Source [32], modified

In this work a different approach to the detection of isotopes with trace level sample abundances as well as when interfering background is presented. We propose an AMS, combined with time-of-flight measurements, using a passive absorber or a gas-filled magnet for isobar suppression.

3.2. MLL Accelerator Mass Spectrometry (AMS) facility in Garching

The main problem in the measurement of some isotopes, additionally to their trace level concentrations, is the isotopic, isobaric and molecular background. That is why the AMS earned a special place among the detection techniques. This is an extremely sensitive method for detection of long-lived radioisotopes. It has also the ability to separate a rare isotope of interest from the abundant neighbouring mass in a unique way. Due to the higher accelerating energies compared to the conventional mass spectrometers, a significant improvement in the isotopic suppression can be achieved. The stripping process in the tandem terminal destroys the molecular bonds and create ions leaving the accelerator in high

charge states. An additional advantage is the usage of the less sample material without losing sensitivity and accuracy.

The AMS structural components are described in the following sections for the example of the tandem accelerator facility at the MLL in Garching, presented on Figure 3.1.

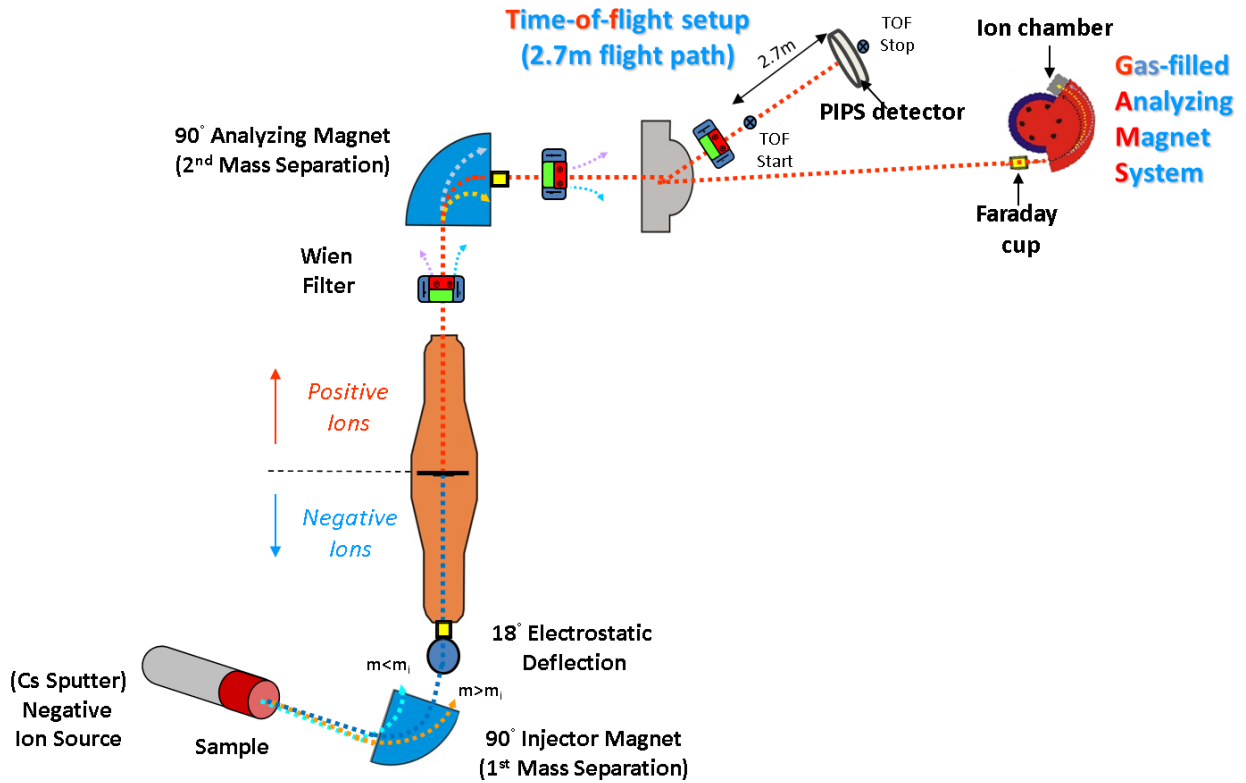


Figure 3.1. AMS set-up at MLL in Garching.

The accelerator mass spectrometry set-up consists of a low energy side, including ion source, injection magnet and electrostatic deflector, as well as high energy side, including tandem accelerator, analysing magnet and successive ion filters. The different components and their contribution to the background suppression will be discussed in the following sections.

3.2.1 Ion source

Due to the utilisation of a tandem accelerator and considering its functional principle a negative ion source is needed.

For the measurements a caesium sputtered negative ion source was used. The geometry of the source is schematically shown in Figure 3.2, which corresponds to a modified Middleton type ion source with a spherical ionizer [34].

With AMS a great variety of materials can be measured. In most cases, in order to obtain a measurable sample, they have to undergo a prior chemical extraction and preparation. The ready sample material is also usually mixed with silver or copper in order to increase the thermal and electrical conductivity, if the material itself has very low conductivity characteristics. The ready sample material is hammered into a holder, mounted onto a water cooled cathode and introduced in the source (Figure 3.2). Caesium from a reservoir is vaporised and enters the enclosed cavity between the cathode and ionizer. The ionizer itself presents a heated semi spherical tantalum surface reaching temperatures in the order of 1000°C [35]. The work function of tantalum is higher than the ionisation energy of caesium [35], which enables the ionisation of the caesium vapour, and the formation of positive ^{+}Cs ions. As the cathode lies on a lower potential than the ioniser the ^{+}Cs ions are accelerated towards the sample, sputtering it. In this way negative and positive ions as well as neutral atoms will be sputtered from the sample surface. The negative ions are accelerated towards the extraction electrode due to the negativity of the cathode. The positive particles stay in the sample and could be used further for sputtering. The neutral ones remain in the source. Furthermore, a thin layer of caesium is formed on the sample surface because of the condensation of the hot Cs vapour on the water cooled cathode. This layer also considerably helps the formation of negative ions.

The negative ion source has some advantages considering isobar suppression of the isotope of interest. Some isobars can be avoided, because they have a negative electron affinity and do not form negative ions. Examples are the completely suppressed $^{14}\text{N}^{-}$, $^{26}\text{Mg}^{-}$, $^{55}\text{Mn}^{-}$, $^{129}\text{Xe}^{-}$ while detecting ^{14}C , ^{26}Al , ^{55}Fe and ^{129}I respectively. Unfortunately, in the case of ^{93}Zr , its isobar ^{93}Nb has also positive electron affinity and builds negative ions so it cannot be suppressed in the ion source. Yet, The Nb isobar can be suppressed to a certain extend depending on the sample material. For the current experiments ZrO_2 was used, hammered into a Cu holder. The reason to use Cu and not Ag, which was also available, is that Ag builds negative ions with the same mass 109 as the $^{93}\text{Zr}^{16}\text{O}$. This results in high currents for this mass, not resulting from the isotope of interest. Additionally, sample material with ZrF was also utilized in order to compare the suppression of ^{93}Nb in the source. Unfortunately, these and previous measurements [20] have shown that even a good candidate for Nb suppression, ZrF delivers very low ion currents and is a matter of some difficulty during the measurements.

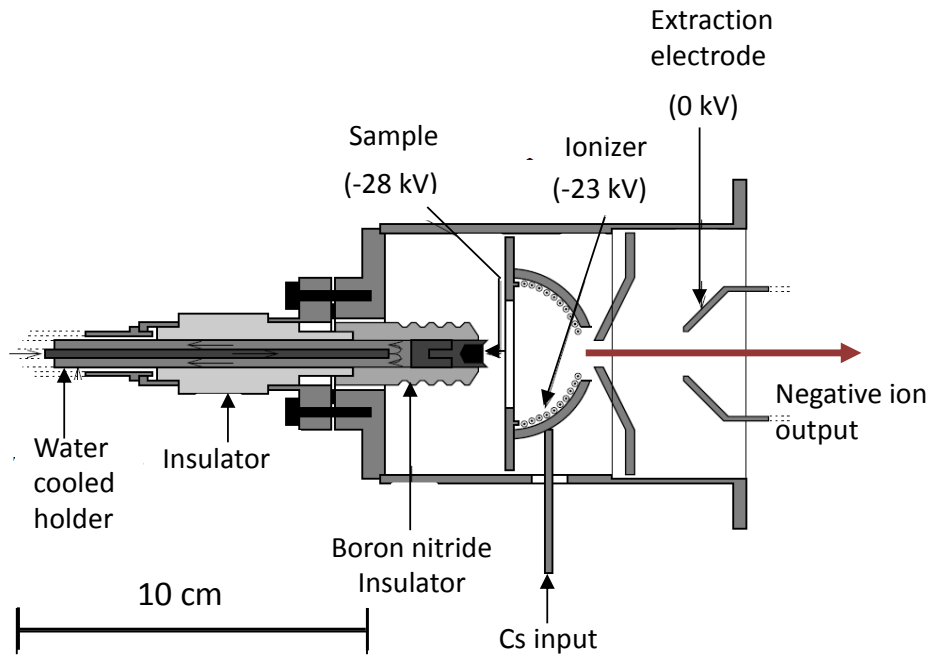


Figure 3.2. Ion source, modified Middleton type. Source [34], modified

3.2.2. Injector magnet

The negative ions leave the ion source with an energy corresponding to the potential between the cathode and the extraction electrode. The potential is fixed to 28 kV, so for a singly charged negative ion or molecule, for which sometimes higher currents are obtained, the energy will be 28 keV. Afterwards the ions enter the 90° dipole injector magnet. This is the first mass separation stage, functioning as a conventional mass spectrometer, and also part of the particle injection system into the tandem.

The negatively charged ions coming from the source enter the magnet and undergo a deflection due to the Lorentz force. The particle will feel an acceleration perpendicular to both the magnetic field lines and the velocity vector and will follow a circular path. Considering the magnetic rigidity, Equation (3.1), one can determine the radius of the mass of interest:

$$B \cdot r = \frac{p}{q} = \frac{\sqrt{2mE}}{q} \quad (3.1)$$

where B is the magnetic field, r is the radius of flight path curvature, p and q are the particle's momentum and charge respectively, m is the mass of interest and E the energy of the ions.

The energy is constant and, as mentioned before, for a single negatively ionised particle is 28 keV, the charge q is going to be the elemental charge of $e = 1.602 \cdot 10^{-19}$ C. Thus, altering the magnetic field leads to a change in the curvature radius. The mass of interest will exit on the other side of the magnet and be guided to an electrostatic deflector. The neighbouring masses will be deflected with different curvature radius, thus, will be stopped on the slits on the exit of the magnet.

One should have in mind that setting the magnetic field to transmit a certain mass allows also the transmission of all background with the same mass. For the example of $^{93}\text{Zr}^{16}\text{O}^-$ the background from ^{109}Ag cannot be suppressed.

Also the limit in the resolution of the “ion source – magnet system” should be taken into account. For medium mass ions it is impossible to select only one mass for transmission. Instead, a Gaussian distribution on the magnet exit is obtained. Measuring the full width at half maximum (FWHM) of this distribution, the magnet resolution can be calculated to be

$$\frac{\Delta m}{m} = 2 \cdot \frac{\Delta B}{B} \approx \frac{1}{300} \quad (3.2)$$

3.2.3. Tandem accelerator

The accelerator used for the measurements was a 14 MV tandem accelerator. The following relation is directly utilized

$$E = q \cdot e \cdot U \quad (3.3)$$

where E is the electrical field, q is the integer charge state of the atom and U is the applied voltage. In order to form an electric field in the terminal (Figure 3.3) positive charges are transported from ground potential to the terminal via isolating chains. In order to achieve higher voltages and respectively higher ion energies, the accelerator is enclosed in a solid metal tank with an isolating gas of high electrical strength – SF_6 .

The advantage of the tandem accelerators is that they use the terminal voltage twice. The ions entering the tandem are negative, not positive. They are accelerated towards the positively charged terminal, located in the middle of the accelerator tank. In the terminal a thin carbon foil is placed with surface density of $4 \mu\text{g}/\text{cm}^2$. Passing through this foil the negative ions are stripped of some of their electrons and in this way positive ions are formed. This positive ions are accelerated again, repelled from the positive potential of the terminal, towards the ground potential of the accelerator exit. Additionally, the passage through the

carbon foil destroys the molecular bonds, which leads to suppression of molecular background.

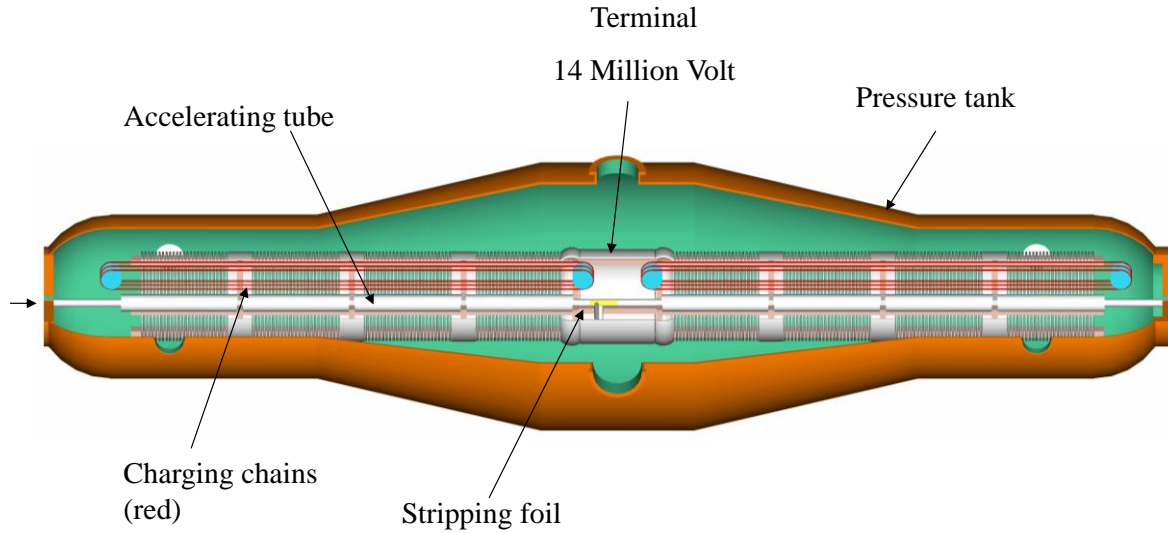


Figure 3.3. Structure of a tandem accelerator. (Courtesy of Peter Hartung)

The ion charge state distribution after passing through the stripping foil can be approximated in average using the Bohr Adiabatic Criterion [36]. It states that the electrons with orbital velocity smaller than the velocity of the ion itself relative to the medium of propagation have higher probability to be stripped off after collision with the target atom. Detailed calculations can be found in [37] [38]. Still, this criterion is with limited validity.

The charge state, q , also determines the final energy of the ions, leaving the accelerator, which can be described with the following formula:

$$E_f = \frac{m_{ion}}{m_{molecule}} \cdot E_{PA} + \left(\frac{m_{ion}}{m_{molecule}} + q \right) \cdot e \cdot U_T \quad (3.4)$$

In this equation E_f denotes the final ion energy, E_{PA} the energy of the ions after the pre-acceleration stage at the entrance of the tandem and U_T the terminal voltage. In the case of the use of molecules and considering Equation (3.4) one can easily see that the final energy of the ion of interest is higher when the mass of the molecule, entering the tandem accelerator, is lower. That is why it is suitable to use lighter molecules containing the isotope of interest. Additionally, higher charge states can be chosen in order to increase the acceleration, but the corresponding charge state yields should be taken into account. For a

certain terminal voltage there is a charge state, having the highest probability to be produced and also the potential to deliver the highest ion current in comparison to the other states.

3.2.4. Beam transport

After the accelerator, an analysing magnet is positioned. Its functioning principle is similar to the one of the injector magnet. However, the mass resolution of this magnet is much higher and lies in the order of $\Delta m/m \approx 10^{-4}$. Usually the magnetic field of this magnet is kept constant and ensures the constant magnetic rigidity of the ions in order to avoid variations due to hysteresis in the magnetic elements. Thus, during a measurement session with several isotopes of interest the terminal voltage, the electric fields of the Wien filters and also the magnetic field of the injector magnet have to be changed and adjusted accordingly.

In the analysing dipole magnet one selects a suitable combination for the experiment from mass, energy and charge, following the formula $m \cdot E^2/q^2$ or simplified p/q – momentum over charge. Unfortunately, ions and molecular fragments with the same magnetic rigidity $B \cdot r = p/q$ also pass the magnet. That is why on the high energy side of the AMS set-up two Wien filters are located with an additional one on the Time-of-flight beam line (see Chapter 3.3.1).

A Wien filter is a velocity filter, sorting the particles according to their E/m ratio. The structure of this filter resembles the one of a plate capacitor, placed in a uniform magnetic field normal to the electrical field lines. Both fields are oriented perpendicular to the particle velocity vector on the entrance window. A positive particle coming from the accelerator and entering the Wien filter feels a force, resulting from the electrical field and proportional to the charge and field itself. The magnetic field B exhibits a Lorentz force on the particle, bending its trajectory in the opposite direction to the one from the electric field E . Only for selected mass and velocity these two forces will be in equilibrium and the particles will fly straight through the Wien filter, fulfilling the formula:

$$\vec{v} \times \vec{B} = \vec{E} \quad (3.5)$$

In this way, the isotopic background can be further rejected and thus suppressed on the detector at the end of the beam line. Particles with different mass or velocity will be deflected and blocked from a collimator, a pair of slits, after the Wien filter. The position of the collimator compared to the unwanted ion displacement at the same position can also have a role in the resolution capability of the Wien filter. In the next table the resolutions of the three Wien filters are listed, showing the low separation capability of the second one.

	Resolution
Wien filter I	1/40
Wien filter II	1/10
Wien filter III	1/100

Table 3.2. Resolution of the three Wien filters.

3.3. The AMS set-ups

The described mass separation equipment in the previous section suppresses the isotopic background of the isotope of interest. Unfortunately, in many cases, a stable isobar is present in the sample. For ^{93}Zr this is ^{93}Nb , which is a stable isotope with an abundance of 100%. This requires an additional isobar separation which takes place in the Time-of-flight beam line (TOF) or with the Gas-filled analysing magnet system beam line (GAMS). For positioning of the beam lines see Figure 3.1.

3.3.1. GAMS beam line

The analysing magnet system contains a gas-filled magnet and an ion chamber as detector. The ions coming from the accelerator have the same magnetic rigidity and could not be filtered through the analysing magnets. Together with the ions of interest an isobaric background is present, so a detector has to distinguish them. Also, a small amount of interfering isotopes still exists in the ion beam. On this place the properties of the gas-filled magnet are of great importance for isobaric background separation.

The GAMS consists of a 135° dipole magnet with bending radius of 0.9 m. The magnet chamber, separated from the vacuum in the beam line through a $0.9\ \mu\text{m}$ Mylar foil, is filled with nitrogen gas having pressure of around 4 – 5 mbar. The high energy ions undergo numerous collisions with the nitrogen atoms in the magnet and as a consequence their charge state is changed. If the same consideration is applied as in the section for stripping the negative ions in the tandem, the Bohr criterion can be used, with some limitations, to determine the average charge state. However, a better prediction can be obtained by the Sayer formula [39], representing the heavy ion stripping probability.

$$\bar{q} = Z_1 \cdot (1 - 1.08 \cdot \exp[-80.1 \cdot Z_1^{-0.506} \left(\frac{v}{c}\right)^{0.996}]) \quad (3.6)$$

The quantities in this equation are as follow: Z_1 – the atomic number of the projectile, v – projectile's speed and c – speed of light. The magnetic field in the magnet assures the different deflection of different ions caused by the Lorentz force. As the formula for the magnetic rigidity, Equation (3.1), still holds in the conditions of the gas-filled magnet, the isobars obtain different rigidity due to the different charge state.

For the example of the isobars ^{93}Zr and ^{93}Nb , calculations using the Sayer formula were performed. The two isobars have different atomic number (Z_p) and thus they obtain different average charge states resulting in different magnetic rigidity. This is presented in Figure 3.5. Keeping the magnetic field constant, it can be seen that ^{93}Zr has higher rigidity resulting in bigger radius in comparison to ^{93}Nb . The isobaric background from ^{93}Nb can be eliminated, or in the real case significantly reduced, by closing the slits on the exit side of the gas-filled magnet.

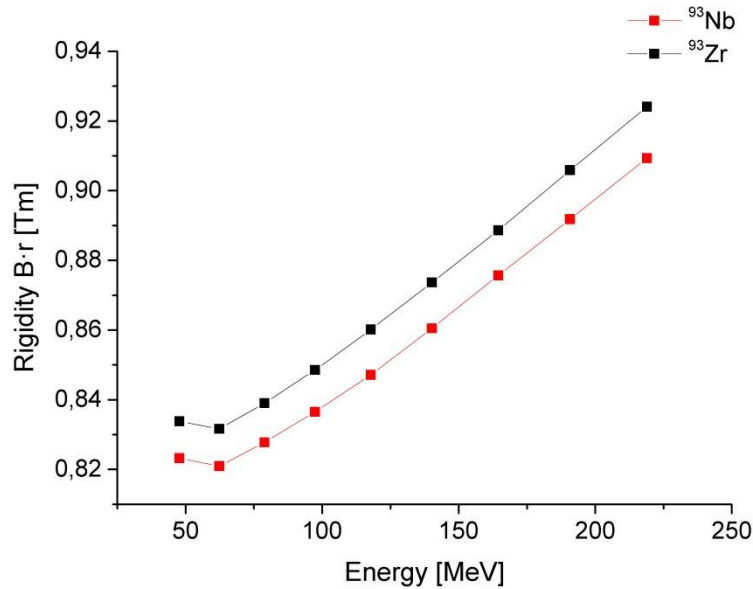


Figure 3.5. Magnetic rigidity calculation, using the Sayer formula. It can be noticed that the rigidity of ^{93}Zr changes only by 10% over an energy range, increasing with a factor of 4.

For detection of the single ions after the gas-filled magnet a Frisch-grid ionisation chamber was used. The detector was filled with isobutane gas. Its pressure, usually around 43 mbar, could be varied with the energy of the incident ions and in accordance to the pressure in the gas-filled magnet. The incident ions lose along their path different amount of energy, specific to the element, due to collision with the gas molecules. Additionally to the magnet, the Frisch-grid detector contributes to the isobar separation. The anode of the ionisation chamber is separated in five energy loss sectors (stripes), Figure 2.6. As it can be seen, the first two stripes are diagonally divided in order to achieve a measurement of the ions entrance position and horizontal incident angle. There is also a possibility to determine the vertical propagation angle by measuring the time difference between the first and the third

sectors. Due to the collisions with the gas in the chamber both isobars will lose different amount of energy and will be stopped on different depth. This is registered from the anode stripes in the Frisch grid. Isobar suppression can be achieved with very high efficiency using the GAMS beam line. In the example of ^{60}Fe , an upper detection limit of this isotope by separation of the background $^{60}\text{Fe}/\text{Fe}$ was achieved to be below 10^{-16} [40].

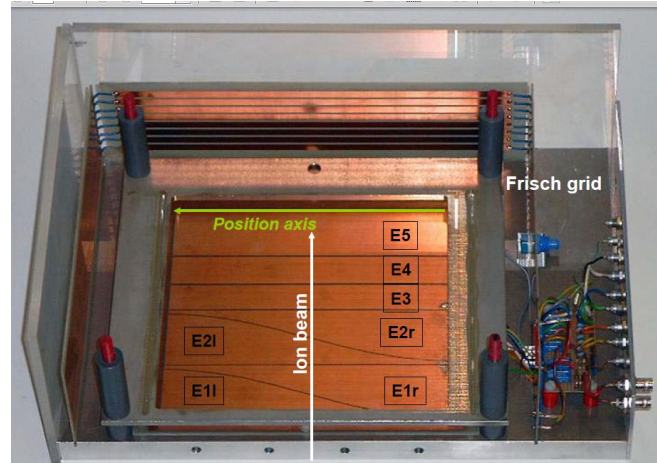


Figure 3.6. Frisch-grid detector scheme.

3.3.2. Time-of-flight (TOF) set-up in the Actinide beam line

The main experiment for isobar background suppression was carried out with the time-of-flight set-up (Figure 3.1). A schematic presentation is given on Figure 3.7.

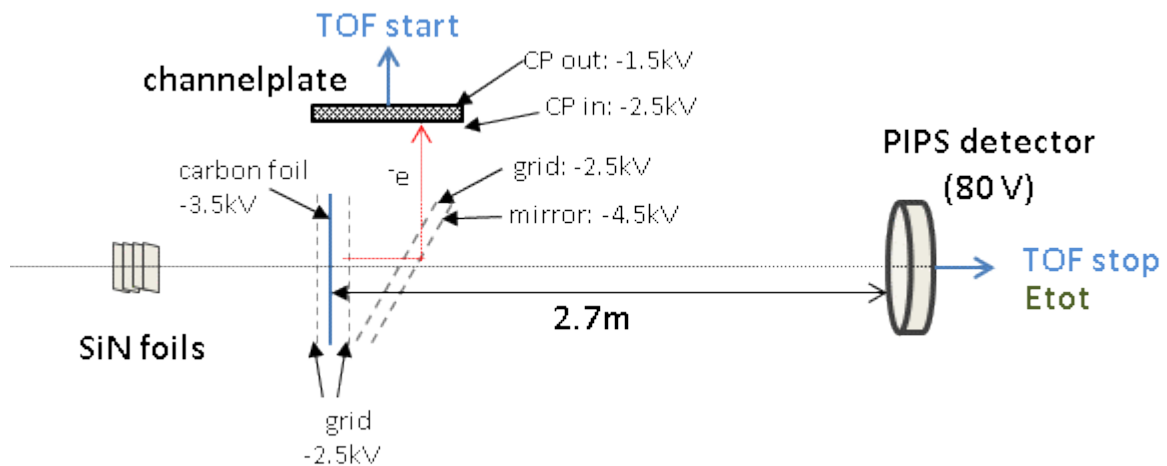


Figure 3.7. Time-of-flight set-up.

With this beam line the time of flight of heavy ions is measured together with their energy. The positive ions travelling through this beam line have to produce a start and stop signals. The start signal is given from a detector, containing a channel plate. The ions pass along their flying path through a carbon foil, typically $7 \mu\text{g}/\text{cm}^2$, and release secondary electrons. They are repelled from the foil towards the surrounding grids, experiencing positive potential gradient in this direction. The electrons reach an electrostatic mirror, which deflects them to the channel plate, where they are detected and generate the TOF start signal. The energy loss of the positive ions in the foil was measured using Bi ion beam and was determined to be $\sim 1\%$. Such loss is small compared to their high energies. Additionally, all considered ions lose approximately the same amount of energy and this loss is not explicitly taken into account.

The ions continue their linear propagation after passing through the carbon foil. After 2.7 m, the length of the time-of-flight set-up, they are stopped by means of a semiconductor detector. The signal from the detector provides information for the final energy of the incident ions as well as triggers the stop TOF signal. After subtraction of the TOF start and stop signals, carried out from the set-up electronics, the time of flight of the heavy ions is determined and can be correlated to the energy. The ions reaching the Time-of-flight beam line have the same magnetic rigidity. It was specified by the analysing magnet after the tandem accelerator. The formula for the magnetic rigidity, Equation (3.1), can be further expanded, using the non-relativistic energy:

$$B \cdot r = \frac{p}{q} = \frac{m \cdot v}{q} = \frac{m \cdot L}{q \cdot \text{TOF}} \approx \frac{\sqrt{2m \cdot E}}{q} \quad (3.7)$$

In this formula L denotes the 2.7 m length of the TOF beam line, m is the mass of the considered isotopes and E their final energy. It should be taken into account that the fourth sign does not represent equality but an approximation [35]. The calculations made and the formulas used are all in the non-relativistic region. The reached ion velocities after acceleration in the tandem are all below the $0.1c$ velocity limit. In the example of ^{92}Zr , the lightest ion used for these measurements, accelerated to 165 MeV has velocity of $0.06c$.

The semiconductor detector used at the end of the beam line was a Canberra Passivated Implanted Planar Silicon (PIPS®) detector. This kind of detector was used for the first time for measuring ^{93}Zr . It was chosen because of its advantages over the silicon surface barrier (SSB) detectors, previously used. They include stability of the entrance window, 8 to 100 times lower leakage current, improving the resolution, and also lower entrance window thickness [41]. For the experiments a partially depleted detector was used with an additional 200 Å aluminium layer – TMPD 450-20-300 AM. This detector provides very good timing resolution [41]. This is of importance, considering the high background at the detection ^{93}Zr isotope. Using the measurements conducted in this thesis, the temporal resolution of the PIPS semiconductor detector was measured to be ~ 380 ps.

To separate the isobaric background a stack of silicon nitride (SiN) foils was installed in front of the time-of-flight path. The basic concept is that due to the different atomic number Z the two isobars, passing through the foils, will lose different amount of energy (see Section 4.1.1). This thesis was dedicated to investigate the possibility and the limits of such a suppression at the example of ^{93}Zr .

3.4. Measurement concepts

For a normal AMS measurement, three types of samples are utilized. These include standards – samples, containing a known quantity of the isotope of interest, blanks – samples without the isotope of interest, and real samples to be measured. Applying a standard into the ion source, the whole AMS set-up transmission can be determined. With a blank sample information for the background can be collected. For the measurements in this work only blank samples were used. These samples were prepared using ZrO_2 mixed with copper in ratio 1:1. The used zirconium material contained natural abundances of the zirconium isotopes. This excludes the detection of ^{93}Zr and delivers high count rates for the two stable isotopes ^{92}Zr and ^{94}Zr . This is used for optimization of the transmission in the AMS set-up and simultaneously delivers information about the background in the detector. The pulse height and TOF signal for the isotope of interest ^{93}Zr can be determined from the positions of the two stable neighbouring isotopes. After finalizing the trials and defining of the most suitable foil thickness a standard was planned to be used for reassertion and confirmation of the results.

In the next paragraphs the practical determination of the concentration of the isotope of interest will be described.

The concentration of the isotope of interest is a parameter corresponding to the ratio of the number of radionuclide ions to that of the stable isotopes. In our case this is the ratio $^{93}\text{Zr}/\text{Zr}$. The current from the stable zirconium is measured via Faraday cup in front of the detector. The detection of the isotope of interest takes place in the detector.

The identification and counting of the ^{93}Zr events in the detector is possible after defining a software cut. The signals from the detector are presented as 2-dimensional plots with axes representing energy and time of flight. A window is set on the area where the counts of the radionuclide are expected. By optimizing the cut all events inside it can be identified as from the isotope of interest and all outside as background. By using a standard sample this area can be directly outlined, following the boundaries of the spot of the isotope of interest. In our case, using a blank, the ^{93}Zr spot is not available. That is why the position and the form of the corresponding cut were determined using ^{92}Zr and ^{94}Zr isotopes. The behaviour of ^{93}Zr regarding time of flight, energy loss and energy straggling is analogous to the one of the two stable isotopes. In this way the position calculations were accepted as accurate. It is also useful in the measurement course to determine also cuts for the neighbouring stable

isotopes ^{92}Zr and ^{94}Zr as well as for the stable isobar ^{93}Nb , also present as impurity in the blank sample in ppb concentration.

3.4.1. Transmission determination

In order to calculate the concentration of ^{93}Zr in the sample, it is important to know how much of this isotope reaches the detector. On the way from the low energy side to the detection system, the ion beam suffers losses. These are caused by the ion passage through the accelerator, the ion production yield for the chosen charge state and also by the transmission in the rest of the beam line. The transmission through the accelerator and on the high energy side can be calculated by measuring the currents from the Faraday cups before and after the segment of interest. In the case of the segment “low energy side – TOF set-up” the transmission throughout the experiment was in the order of 1%.

The next step is to calculate the transmission from the last Faraday cup to the detector. To achieve this, measurements with a stable isotope were used. It is important to mention that typical ion currents in the order of nA can correspond to a count rate over 10^9 Hz in the detector. This will destroy the semiconductor detector. To reduce the intensity of the beam attenuators are inserted on the ion's path. These consist of a tungsten plates with holes of 100 μm diameter. Thus only part of the beam can pass through. There are three plates installed in the beam line – two with attenuation ratio 1/1200 and one with 1/33.

First, the current of a stable isotope is measured with the Faraday cup in front of the time-of-flight set-up. Using ^{92}Zr , $\bar{I}_{92\text{Zr}}$ presents the averaged current reading before and after the measurement.

After that, the physical transmission of the system is determined, following the formula

$$T_{phys} = \frac{R_{det}}{R_{cup}} \quad (3.8)$$

The term R_{cup} is the rate at the Faraday cup. It is calculated by dividing the averaged current reading for the stable isotope by the elementary charge e and the charge state of the ions q . Additionally, the attenuation factor A should be taken into account.

$$R_{cup} = \frac{\bar{I}_{92\text{Zr}}}{A \cdot e \cdot q} \quad (3.9)$$

In Equation (3.8), the term R_{det} stands for the number of ^{92}Zr ion counts in the detector, $N_{92\text{Zr}}$, during the measurement time t .

$$R_{det} = \frac{N_{92\text{Zr}}}{t} \quad (3.10)$$

With the help of these equations the physical transmission to the detector can be calculated as:

$$T_{phys} = \frac{N_{92Zr} \cdot e \cdot q \cdot A}{t \cdot \bar{I}_{92Zr}} \quad (3.11)$$

Typical values for the physical transmission are 30 – 50% for 0 foils and ~1% for 4 foils.

3.4.2. Concentration of ^{93}Zr

Additional to the physical transmission, the software transmission, T_{soft} , should be determined. It is of importance only when foils are inserted in the beam path. The T_{soft} calculation is explained with the help of Figure 3.8.

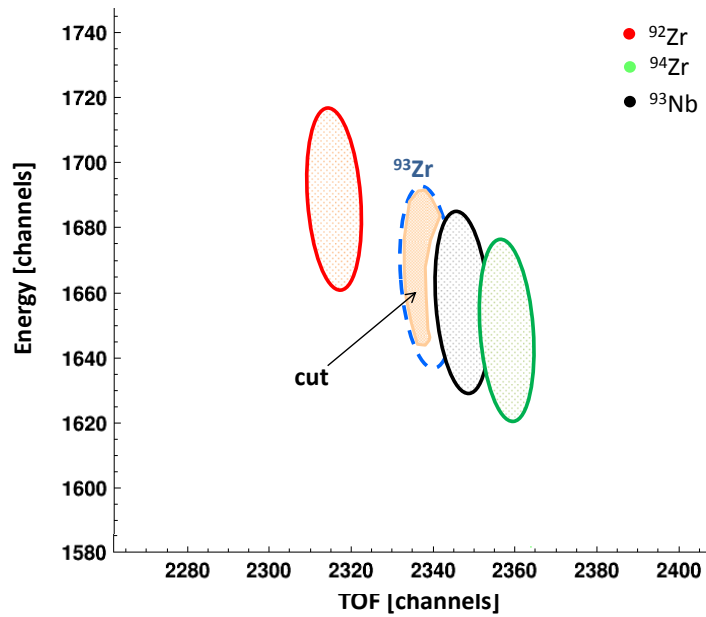


Figure 3.8. Formation of a “cut” for the example of a measurement with 3 SiN foils used for calculation of the software transmission. The blue circle represents the interpolated position of ^{93}Zr .

As seen on Figure 3.8, the position of ^{93}Nb and the calculated position for ^{93}Zr in the plot are partially overlapping. The counts detected in the blue circle cannot be all straightforward related to one of the two isobars. That is why a software 2D cut is defined in which the events can be recognised with high probability as ^{93}Zr . Usually, the cut comprises approximately 40% of all counts in the interpolated ^{93}Zr area. In order to calculate the software transmission, the cut should be applied in the same way on one of the stable isotopes. The resulting counts are divided by the total events from this isotope. As ^{92}Zr is used

for current measurements, the cut is translated onto the corresponding position of the ^{92}Zr area. The software transmission is then calculated as:

$$T_{soft} = \frac{N_{92\text{Zr in cut}}}{N_{92\text{Zr}}} \quad (3.12)$$

The overall transmission from the Faraday cup to the detector is formed as

$$T_{total} = T_{soft} \cdot T_{phys} \quad (3.13)$$

Using equations (3.8 - 3.13), a concentration of $^{93}\text{Zr}/\text{Zr}$ in a sample can be determined even if no standard material is available. It is calculated as the ratio from the events of ^{93}Zr to the effective charge detected in the detector, calculated via the formula:

$$Q_{eff} = \frac{\bar{I}_{92\text{Zr}} \cdot t'}{A' \cdot T_{total} \cdot e \cdot f_{92\text{Zr}}} \quad (3.14)$$

In Equation (3.15) the terms t' and A' denote the time and the attenuators value during the measurement of the isotope of interest ^{93}Zr and $f_{92\text{Zr}}$ stands for the natural abundance of ^{92}Zr (17.15%). Finally, the concentration C is determined via

$$C_{93\text{Zr}} = \frac{N_{93\text{Zr}}}{Q_{eff}} = \frac{N_{(93\text{Zr})sample}}{N_{(\text{Zr})sample}} \quad (3.15)$$

The outlined calculation of the concentration is described for the example of the stable isotope ^{92}Zr . The same result will be also obtained if the stable ^{94}Zr is used.

3.4.3. Error considerations

The experimental measurements are related unavoidably with errors. One of the uncertainties comes from the measured particle current. The error is caused from the averaging of the current readings before and after each measurement. Such approximation doesn't provide optimal description of the real current change, which is not necessarily linear. Another error source during the current measurements is the fluctuation of the current during readout. Long term fluctuations contribute also to the inaccuracy. In some cases the deviation reaches more than 10 % , thus cannot be noted correctly. This error source was taken into account by the calculations for concentration and detection limit determination.

On the side of the detector system, complications are caused by the ions, which arrive simultaneously in the detector. Two ions of the same kind can lead to a signal twice higher than the one from the single event. Still, a distinction should be made according to the arrival time of the ions. If the two events are simultaneous, the electronic system is not capable to distinguish them and they are not discarded. If there is a time span of 0.1-5 μs , then the signals can be rejected via the generation of a pile-up signal from the electronics. Too high count-rates in detector caused by too much background would impede the pile-up formation. This can be avoided by changing the charge state for the measurement.

4. Stopping power and isobar separation

The topic in this thesis is the detection of trace concentrations of ^{93}Zr . The isotope interferences, ^{92}Zr and ^{94}Zr , can be successfully reduced by the different magnetic elements along the beam line. The isobaric interference from the stable isotope ^{93}Nb still exists and prevents the accurate detection of ^{93}Zr . That is why a passive absorber was examined as a possible solution to this problem.

4.1. Heavy ions in matter

The starting point for the theory of heavy-ion stopping is considered the Niels Bohr's classical theory of charged particle stopping, dated from year 1913. In this theory Bohr adopts the Rutherford model of the atom. With the development of quantum mechanics the theories of Bethe, Bloch and Møller were developed, based on the quantum theory of particle stopping in matter. Currently, one of the most developed and researched areas is the stopping of light particles as electrons and protons. Bethe can be considered a pioneer in this field with his work from the year 1930. Unfortunately, the field of stopping of heavier ions is dominated by fitting procedures and extrapolations of experimental data [42].

What makes the difference between the passage of light and heavy ions through matter? The light particles, penetrating a medium, are considered to interact via the relatively weak Coulomb force with the atoms in the medium. This allows the usage of the quantum mechanical perturbation theory, a well advanced concept for solution of such problems. On the other hand, the passage of a heavy ion through a medium cannot be considered as a small perturbation of the target but a strong intrusion. The heavy ions are usually composite particles, which carry electrons. An exception is at very high speeds when the ions are completely stripped of their electrons. Here, one faces the many-body problem, considering the interactions of the incident ion with the bound and free electrons of the target medium.

The key concept in the treatment of the ion passage through matter is the stopping power. It is defined as the energy loss of the incident particle – projectile, per unit length in the target material, expressed with the following formula:

$$S = - \frac{dE}{dx} \quad (4.1)$$

Rewriting equation (4.1), the final energy E_f of the ions after a target of thickness d can be obtained:

$$\int_{E_0}^{E_f} \frac{1}{S(E)} dE = \int_0^d dx = d \quad (4.2)$$

The stopping power has the dimension of a force:

$$[S] = \frac{kg \cdot m}{s^2} \quad (4.3)$$

Despite this controversy, in the literature the term stopping power is adopted.

Considering the energy loss processes active during charged projectile-target interaction, the following processes can be distinguished [43] [44]:

1. Internal charge state of the target changes, expressed in excitation and ionization of the target electrons (bound or in electronic gas);
2. Internal charge state of the incident ion changes, including electronic excitation, ionization and charge state;
3. Nuclear stopping, consisting of the energy transfer to the target ions;
4. Emission of electromagnetic radiation;
5. Chemical and nuclear reactions with the target.

As a summary the interactions can be grouped into electronic and nuclear. The projectiles can be divided in three groups according to their atomic mass number following $Z \leq 2$ light ions, $3 \leq Z \leq 18$ intermediate and $Z \geq 19$ heavy ions [43]. As the considered projectiles in this work have atomic numbers higher than $Z = 19$ ($Z(\text{Zr}) = 40$, $Z(\text{Nb}) = 41$), the focus falls on the heavy type ions. In the case of heavy ions, processes including electronic interactions cannot be neglected. Process 2 gains high importance. In this way it can be shown that for heavy ions the electronic stopping plays bigger role than the nuclear stopping.

The incident ions can be also classified according to their energies. Three regions are differentiated as shown on Figure 4.1. As criterion the ratio E/A is used, which describes the kinetic energy per atomic mass unit of the projectile. This classification is also consistent with the Bohr kappa criterion

$$\kappa = \frac{2 \cdot Z \cdot v_0}{v} \quad (4.4)$$

where Z is the atomic number and v is the speed of the projectile, v_0 is the Bohr velocity.

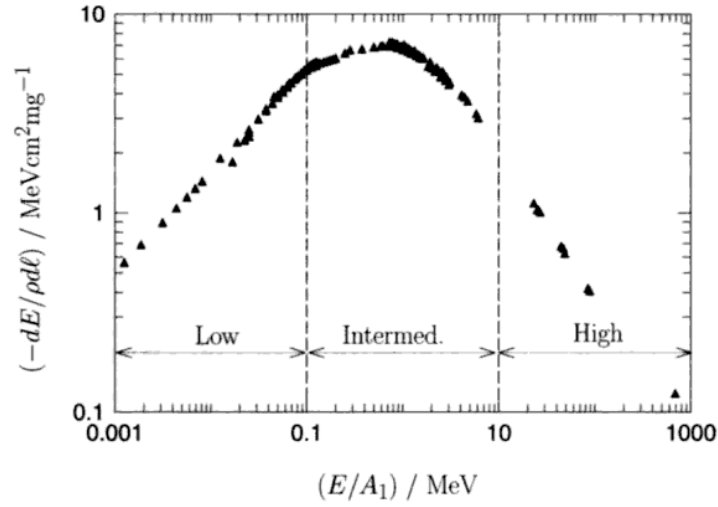


Figure 4.1. Heavy-ion stopping regimes in the example of oxygen projectiles in an aluminium target. Source [44].

For an E/A ratio smaller than 100 keV the incident ions are classified as slow. In this low speed regime the velocity of the projectile is lower than the orbital velocities of the target electrons with exception of the outer ones. In this energetic region the stopping power of the incident ion is considered proportional to the speed. Theory and estimations for the low speed regime can be found in the works of Lindhard and Scharff [45], as well as of Firsov [46].

The region $100 \text{ keV} \leq E/A \leq 10 \text{ MeV}$ is considered as an intermediate regime. The treatment of the intermediate energy range occurs using the Bethe stopping power formula but adding some corrections, concerning for example the effective ion charge. Significant insight of this theory provides the work of Nortcliffe [47].

The region for a specific energy $E/A > 10 \text{ MeV}$ is defined as high speed regime. For such energies the Bethe formula [48] gives an accurate characterisation of the energy loss. Bethe's theory applies in the cases of completely ionized particles. Because of the high velocities in this region the projectiles can be considered as completely ionized. This is supported also by the Bohr kappa criterion, which in this regime is $\kappa \ll 1$. This shows that the orbital velocity of the electrons is much smaller than the velocity of the projectile, so according to the Bohr stripping criterion, this electrons will be stripped.

For the experiments conducted in this thesis the projectiles had energies in the order 80 - 170 MeV (Chapter 5.1.3), which results in 0.9 – 1.8 MeV/amu. After passage of the ions through the stack of foils, their energy was reduced to 20 – 80 MeV, corresponding to 0.2 – 0.8 MeV/amu. This places the experimental results and the considerations for the stopping power in the intermediate regime. As mentioned before, it can be described using Bethe formula with some modifications.

4.1.1 Stopping power

The classical theory considering the stopping power is the one developed by Bohr. In his classical treatment of the problem he adopts the Rutherford model of the atom. Each electron of the target atom is considered as oscillators, having characteristic frequency ω .

In this theory an important place has the impact parameter b , according to which the interactions between the projectile and the target are divided into close and distant collisions. The close collisions, with small b , are described via Coulomb scattering of the incident ion on the electrons in the target material, treated classically. The interaction is not elastic and an momentum transfer, T , takes place. The electron binding is not taken into account. To express this transfer the Rutherford formula can be used [43]:

$$T = \frac{2 \cdot q_1^2 \cdot q_2^2}{m_2 \cdot v^2 \cdot b^2} \left(\frac{1}{1 + (q_1 \cdot q_2 / \mu \cdot v^2 \cdot b)^2} \right) \quad (4.5)$$

The terms are as follow: q_1 , m_1 and q_2 , m_2 are the charge state and mass of the incident ion and the target atoms respectively, b is the collision impact parameter and $\mu = m_1 \cdot m_2 / (m_1 + m_2)$ stands for the reduced mass. Considering long distance collisions, described by large impact parameters, one can accept that the field of the incoming projectile is uniform and its interaction with the bound electrons in the target results only in adiabatic change of the electronic motion. This can be illustrated considering that one target electron orbits many times the nucleus during the collision time. The momentum transfer is considerably smaller than in close collisions and the binding energy of the target electrons should be considered. Detailed description of Bohr, Bethe and Bloch stopping power calculations can be found in [49] [50].

The Bohr theory can be summarized as dependent on the impact parameter between the projectile and the target atom. His stopping power formula for heavy ions with atomic number Z_1 penetrating a target with bound electrons is presented in Equation (4.6)

$$S = -\frac{dE}{dx} = \frac{4\pi Z_1^2 e^4}{m_e v^2} \ln \left(\frac{C m_e v^3}{2\pi Z_1 e^2 v} \right) \quad (4.6)$$

In this equation Z_1 is the atomic number of the projectile, e – the elementary charge, m_e – the mass of an electron and v is its frequency. The constant C equals 1.1229.

A quantum mechanical consideration of the stopping power problem was provided by Bethe, using the first Born approximation, including the quantisation of the physical system. The Bethe's approach examines the energy loss in the light of wave mechanics. There, the Bohr's theory of the impact parameter cannot be applied directly because the close collisions cannot

be quantized using this concepts. This is due to the quantum mechanical restriction for a particle with defined momentum to have defined spatial position [51].

Additional work from Bloch led to unification of the classical theory of Bohr and the quantum-mechanical approach of Bethe. The non-relativistic Bethe-Bloch formula is presented in Equation (4.7):

$$S = -\frac{dE}{dx} = \frac{2\pi Z_1^2 m_1 e^4 Z_2}{E_1 m_e A_2} \rho_2 N_A \ln \left(\frac{2m_e E_1}{I m_1} \right) \quad (4.7)$$

Additionally to the terms emerging in the Bohr equation, in this formula the following quantities are included: m_1 is the mass of the projectile and the target electron; Z and E are atomic number and energy of the projectile, denoted with subscript 1, and the target atom, with subscript 2; A_2 is the mass number of the target material. The terms N_A , ρ_2 and e stand for the Avogadro number, the density of the target and the elementary charge.

The Bethe formula was derived in the case of projectiles with very high velocities, much higher than the orbital velocities of the electrons and thus describes bare ions. For lower incident velocities the projectile is not bare but with electrons circling around the positive core. This additional consideration brings new effects that should be taken into account as screening and antiscreening.

The orbiting electrons alter the interaction of the projectile with the target. The electric field strength of the incident ion and thus its interaction with the target electrons is reduced. This results also in reduction of the stopping power. The representation of the projectile as a composition of particles, interacting separately with the target electrons, leads also to the other effect of antiscreening. The stopping power is enhanced.

Taking into account the electrons around the nuclei of the incident ion and the screening they provide, a justifiable step is to introduce the concept of effective charge. It was defined by Nortcliffe [47] as

$$q_{eff} = \gamma Z_1 \quad (4.8)$$

where γ is the effective charge parameter. The quantity q_{eff} can be also determined from the ratio between the stopping power of known particle, proton or alpha particle, and the stopping power of the considered ion:

$$q_{eff}^2 = \frac{S_{ion}}{S_{proton}} \quad (4.9)$$

Via Equation (4.9), substituted in Equation (4.8), the effective charge parameter can be determined.

If the screening is very high, a lot of orbiting electrons, the classical perturbation theory can be used to describe the interactions. The problem screening can be solved applying a suitable interaction potential and an additional inverse-Bloch correction [44].

4.1.2. Interaction with target and straggling

An essential part of energy loss measurements is the concept of the energy and angular straggling. Considering a collimated ion beam with well specified energy, the passage through a target material causes broadening in the residual energy and the spatial distribution of the beam. This broadening affects the detection resolution and thus is very important when considering separation of the isotope of interest from neighbouring isotope and isobar.

The slowing down of ions in matter is a subject of statistical considerations. With respect to the target there are three cases which can be considered. The first one is the case of a thin target. During its transition time through the material, the projectile collides only with a limited number of target atoms. Most of the incident ions will lose small fractions of their momentum (energy) and this will produce a narrow energy loss, registered in the detector. Still, some ions will undergo numerous collisions with the target atoms and will form a tail in the energy distribution in the detector towards lower energies. The same consideration can be adopted for the angular broadening of the initially collimated ion beam.

The next case is the one of the passage through a thick target, where the incident beam interacts actively with the target. An average value can be calculated for the energy loss of the projectiles. The energy spectrum then has a Gaussian form [52](basic concepts in [53]), centred on this average energy loss. Considering the angular distribution – it obtains also a Gaussian form, centred on the initial projectile direction.

If a very thick target is used, the third case, the incident ions suffer very high energy losses. The deviations from the Gaussian shape of the energy loss are significant. In order to be described, special approaches should be used [44].

One should note that the transition of the projectile through the target governs different statistical considerations, depending on the mass of the particle. For light ions the most important factor in the collision process is the Coulomb scattering. The situation is different for heavy ions where charge exchange processes can take place. The altering of the charge state and even the charge-exchange processes of the projectile may cause alterations in the energy loss and angular straggling [44]. Additionally, instable beam, electronics or the target itself, if non-uniformity is present, can have an impact onto the measurement.

A basic approach for describing the energy straggling originates from Bohr, where he describes the squared fluctuation of the energy loss Ω . The non-relativistic energy-independent formula is presented in Equation (4.10) [53]:

$$\Omega_B^2 = 4\pi Z_1^2 e^4 Z_2 N \Delta R \quad (4.10)$$

Z_1 and Z_2 are the atomic numbers of the projectile and target atom respectively, N is the atomic density in atoms/volume, e is the elementary charge and ΔR is the absorber thickness. This equation is based on the Rutherford scattering law and does not take into account the binding of the electrons in the target material [54].

Better description of the matter is provided by Chu [55] who calculated the straggling of He ions in a variety of materials. There is also the possibility that the results for He to be correlated and adapted for protons [56]. In order to take into account the dependence on the different target material, the Chu calculations were fitted to the formula

$$\frac{\Omega_{Chu}^2}{\Omega_B^2} = \frac{1}{1 + A_1 E^{A_2} + A_3 E^{A_4}} \quad (4.11)$$

where Ω_B and Ω_{Chu} are the Bohr and Chu fluctuations of the energy loss, A_1 to A_4 are Z_2 dependent fitted coefficients and E is the energy of a hydrogen ion, measured in MeV/amu [56]. Considering statistical fluctuations of the ion stopping in matter and taking into account Equation (4.11) the final Yang formula can be written as [56]

$$\left(\frac{\Omega^2}{\Omega_B^2}\right)_{ion} = \gamma^2 \left(\frac{\Omega_{Chu}^2}{\Omega_B^2}\right) + \left(\frac{\Delta\Omega^2}{\Omega_B^2}\right)_{ion} \quad (4.12)$$

In this equation the γ term represents the effective charge factor, a characteristic of the ions in matter. Additionally, correlation effects are taken into account represented by the term $\Delta\Omega$. The formula is valid for a wide range of ion masses..

For the practical realization the energy straggling was estimated from the output of the SRIM simulation program.

4.1.3. Separation

Following the considerations from the previous chapter and in the context of isobar separation, it is useful to determine what is important for a clear separation of two peaks in the detector.

The energy and TOF detection signals from the ions of a specific isotope are registered as peaks with certain broadening, due to statistical reasons and to the straggling, caused by the passage through the passive absorber for the example of TOF beam line. They can be approximated with a Gaussian distribution in the energy, and respectively time of flight, spectra centred on the average energy loss for the considered foil thickness. Let the distance

between the maxima of two neighbouring peaks be D . The width of each peak can be characterised by the FWHM (full width at half maximum). To distinguish two peaks as two different events requires the fulfilment of the requirement:

$$D \geq FWHM \quad (4.13)$$

Additionally the following ratio can be considered:

$$W = \frac{FWHM}{D} \quad (4.14)$$

The resulting value for W should be as low as possible in order to achieve maximal separation.

This is presented graphically in Figure 4.2 for the example of ^{93}Zr and ^{93}Nb measurements at 140 MeV with 4 foils (see Chapter 5.1.3).

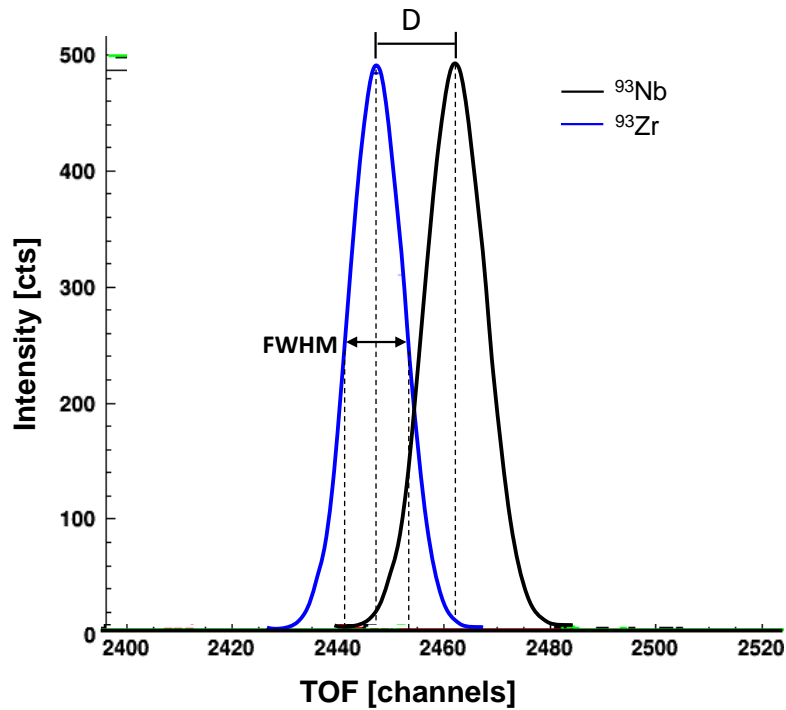


Figure 4.2. Presentation of the separation considerations

4.2. Simulations

4.2.1. Stopping power for mass 93

An expedient step before starting with the measurements was to conduct simulations about the stopping power of ^{93}Zr and ^{93}Nb in the SiN material. The consideration of the Bethe-Bloch formula was one of the points, according to which ^{93}Nb , having higher atomic number Z , will lose more energy in the material and thus will have higher stopping power. The available simulation programme SRIM by Ziegler (2011), [51], was used in order to plot and compare the stopping power curves. Another source for comparison was the stopping power tables for heavy ions from Northcliffe and Schilling, published 1970 [47]. Unfortunately, in the tables there are no data for SiN target material. That is why the compound formula, Equation (4.15) [44], was used. It represents the Bragg additive rule for n_i number of atoms per volume and the corresponding cross section S_i to the corresponding i -th target atom species

$$-\frac{dE}{dx} = \sum_i n_i S_i \quad (4.15)$$

The results from the SRIM simulation and the Northcliffe and Schilling tables calculations are presented on Figure 4.3.

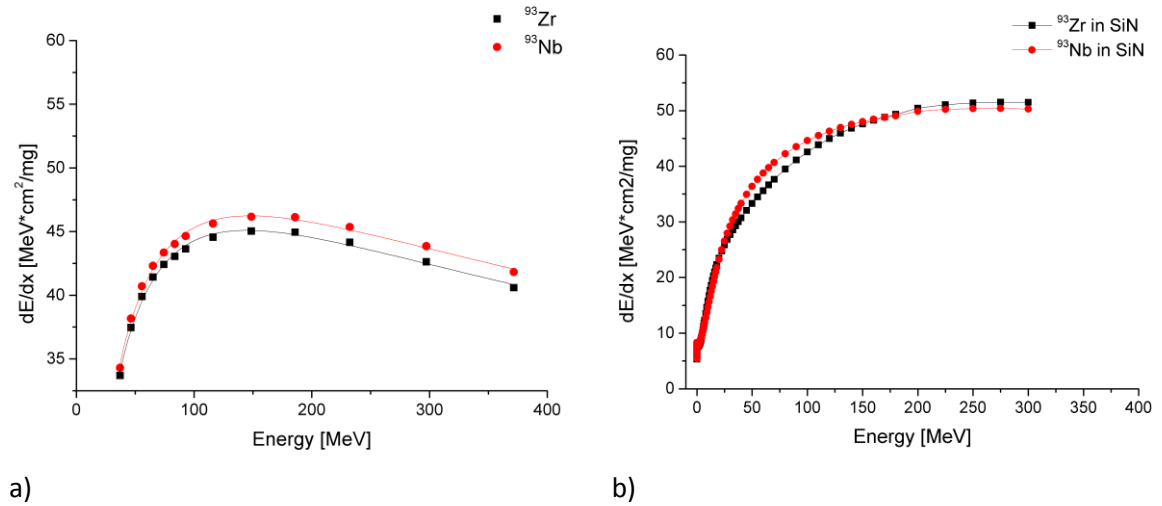


Figure 4.3. Stopping power curves of ^{93}Zr (black) and ^{93}Nb (red), obtained through a) Northcliffe and Schilling tables and b) SRIM simulations

What can be seen from the plots is that the Northcliffe and Schilling tables show a tendency as in the formula from Bethe-Bloch. Niobium, because of the higher Z , has, as expected, higher stopping power. If we restrict our considerations only to this plot then the absorber thickness (number of foils) should be chosen as high as possible. From the figure can also be concluded that the higher the incident energy is chosen the better the separation between the isobars will be due to the maximum energy loss. The highest energy available was ~ 170 MeV, which could be enough to separate the isobars and to register ^{93}Zr as a single peak. An important detail that should be taken into account is the energy and angular straggling, which present an upper limit of the number SiN foils utilized.

The conduction of the SRIM simulation has shown some discrepancies. The stopping power curves for ^{93}Zr and ^{93}Nb are clearly not following the Bethe-Bloch model. Additionally, they have two interception points, marked with red circles, at energies ~ 23 MeV and ~ 165 MeV, which is not physical. In this case a careful analysis of the foil thickness and ion incident energies has to be made. A suitable value for the energy of the ions is the one around the second interception point. The maximum energy loss is expected if using the proper number of SiN foils final ion energy around the first intersection point is reached. Initial energies above 170 MeV would not be helpful, because the difference in the energy loss and thus the difference in TOF is too small. In a personal correspondence, [20], Ziegler gives an explanation for the discrepancy of the models. According to him, the stopping power curve for Nb was obtained using theoretical modelling and its initial position was between the ones for Zr and Mo. Experimental data shifted the Nb curve, but was insufficient to update the other two curves. Ziegler's opinion was that the stopping power data from Northcliffe and Schilling is more trustworthy and should be considered as correct.

Having these two stopping power simulations that differ from each other, it was decided that an experimental verification should be the best way to find the most suitable configuration for isobar separation. Before that, as a test, other simulations were made.

4.2.2. Simulations for ^{87}Rb and ^{87}Sr

The lack of stopping power uniformity in Figure 4.3 led to the suggestion to consider two other neighbouring elements in order to obtain a better picture. The isotopes ^{87}Sr and ^{87}Rb were chosen. The similarity between both is that the isotope ^{87}Rb has very long half-life in the order of 10^{10} a and has also a stable isobar - ^{87}Sr . Yet, in contrast to ^{93}Zr and ^{93}Nb , ^{87}Rb has a stable phase and ^{87}Sr has a decaying phase with very short half-life (2.8 h). The mass difference of ^{87}Sr and ^{87}Rb is also bigger.

The reason why these two isotopes were selected was the assumption of better studied stopping powers and the availability of more precise data in the SRIM stopping power tables. This is supported by the plot on Figure 4.4 where the agreement between the Bethe-Bloch

formula and the SRIM simulation can be clearly seen. The isobar with higher atomic number ^{87}Sr , $Z=38$, loses more energy in the same absorber thickness than ^{87}Rb , $Z=37$. What we would expect is that using higher energy ions and utilizing more SiN foils will lead to better separation. The mass 87 is not far away from the mass 93. What we could expect is that ^{87}Sr and ^{87}Rb would have similar behaviour concerning stopping in the passive absorber, thus the results should also be valid for ^{93}Zr and ^{93}Nb .

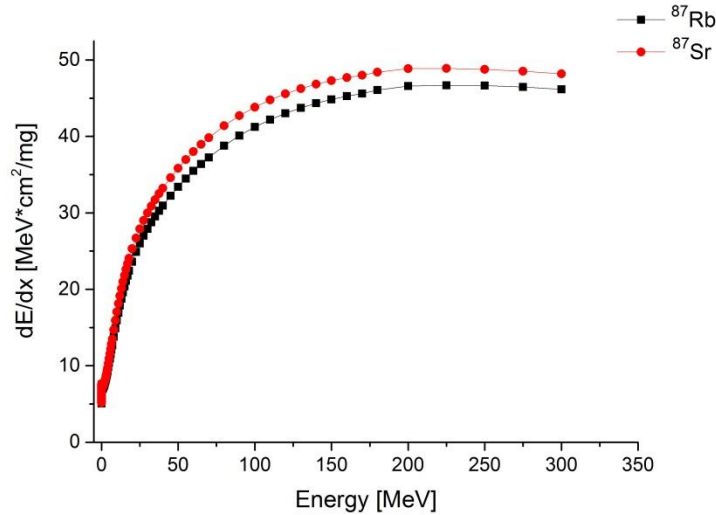


Figure 4.4. Stopping power curves, plotted using SRIM

The parameters considered in the simulation were the thickness of the absorber and the broadening of the peaks after passing through the foils. The values calculated were the distance between the ^{87}Sr and ^{87}Rb TOF peaks and their FWHM. Both are plotted in Figures 4.5 and 4.6 as where on the x-axis is the corresponding number of SiN foils.

From the plots of the FWHM can be noticed that ^{87}Sr , with higher Z number than ^{87}Rb , for an energy of 78 MeV is stopped completely after more than 10 SiN foils, corresponding to 10 μm absorber thickness. For fully stopping the ^{87}Rb ions 11 μm SiN are needed. The increasing width of the peaks and their distance with increasing number of foils is also clearly seen. For optimal separation of the two peaks, according to formula (10.1), the greatest distance between the peaks is needed with the smallest value for the FWHM. An evaluation showed that an acceptable separation can be achieved with 8 foils. Also, the usage of 9 and 10 foils is possible but the straggling from ^{87}Sr becomes an obstacle. Of course, these are theoretical results. For precise prediction experimental results are required.

The atomic numbers of ^{93}Zr and ^{93}Nb are higher. This leads to higher energy loss in the absorber and also more energy straggling. The conclusion could be made that for the optimal isobar separation of ^{93}Zr and ^{93}Nb a maximum of 8 SiN foils should be used.

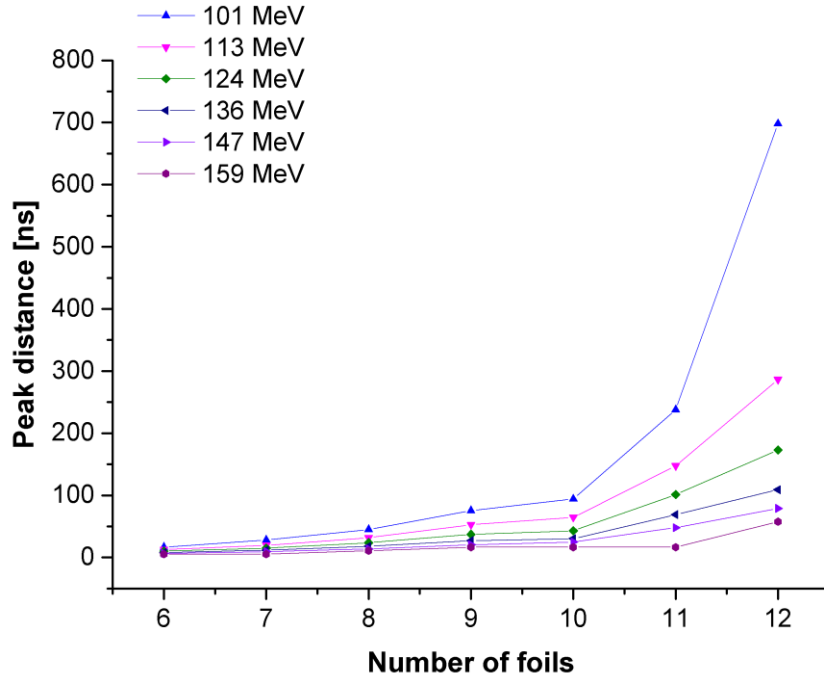


Figure 4.5. TOF distance between the peaks of ^{87}Sr and ^{87}Rb . SRIM simulation for different energies and foil number

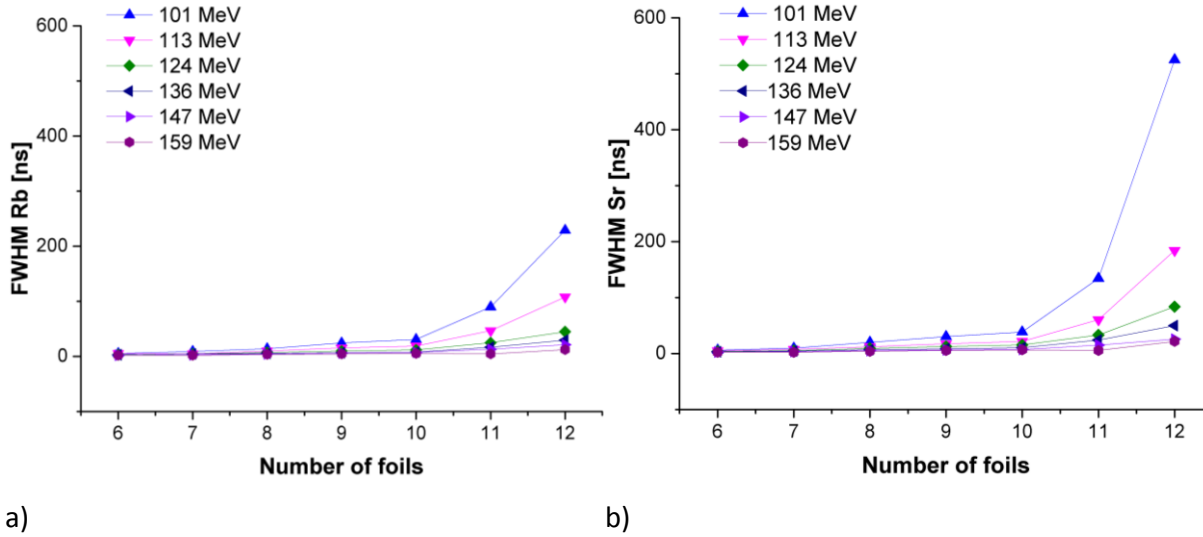


Figure 4.6. FWHM for a) ^{87}Rb and b) ^{87}Sr . SRIM simulation for different energies and foil number

5. Experiment

The experimental AMS part was conducted using the TOF beam-line in conjunction of a stack of SiN foils as passive absorbers. The end energy and time of flight of ions were detected with a PIPS semiconductor detector (see Ch. 2.3.2.). Additionally, a comparative study was conducted using the GAMS beam-line.

5.1. Time-of-flight beam-line

5.1.1. SiN foil set-up

A detailed description of the TOF beam-line was provided in Chapter 3.3.2. As already mentioned, for the isobar separation of ^{93}Zr and ^{93}Nb a stack of SiN foils was installed in front of the TOF set-up. On Figure 5.1 a photo of a single foil is shown, supplied by Silson Ltd.

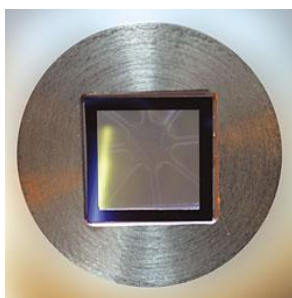


Figure 5.1. Photo of a SiN foil with a frame and holder. Source [57].

The membranes have a stoichiometry close to Si_4N_3 . For the experiments the foil thickness was $1\text{ }\mu\text{m}$. The nominal value of the membrane thickness, determined from the manufacturer was 1038 nm [58]. Thicker membranes are not available from this supplier. The reason is that such foils are not stable due to the large tensile residual stress, accumulating in the material.

One of the methods to produce silicon nitride foils, also used to manufacture the foils for the experiment, is the method of Low Pressure Chemical Vapour Deposition (LPCVD) [58]. This method includes the deposition of nitride ions on a silicon grid using ammonia (NH_3) gas.

The question rises why SiN foils were used. In a previous work [20] a comparison was made between SiN and Beryllium foils. Theoretically, Be foils should be the better choice in stopping power applications. Be has lower atomic number. The simulation and considerations using the Bethe-Bloch formula show that Be should have better passive absorber qualities than SiN. Unfortunately, the measurements could not provide the expected results. The reason is that the theory assumes perfectly manufactured Be foils, which in reality is not the case. The uniformity is restricted and this leads to additional differences, which cannot be precisely predicted. In contrast, SiN foils can be produced with high surface flatness and the uncertainties due to variable thickness become irrelevant.

After pointing out the advantage of the SiN foils, let us show their arrangement in the beam-line. The foils were mounted on trays, fixed on a ladder holder.

We used two trays with two foil configurations in one session. To change the number of foils the TOF beam-line had to be vented. On the positions between the two trays with foils spherical apertures with diameters 2 and 4.3 mm were mounted and used for focusing and collimating the ion beam (Figure 5.2). The ladder had to be manually placed in the desired position.

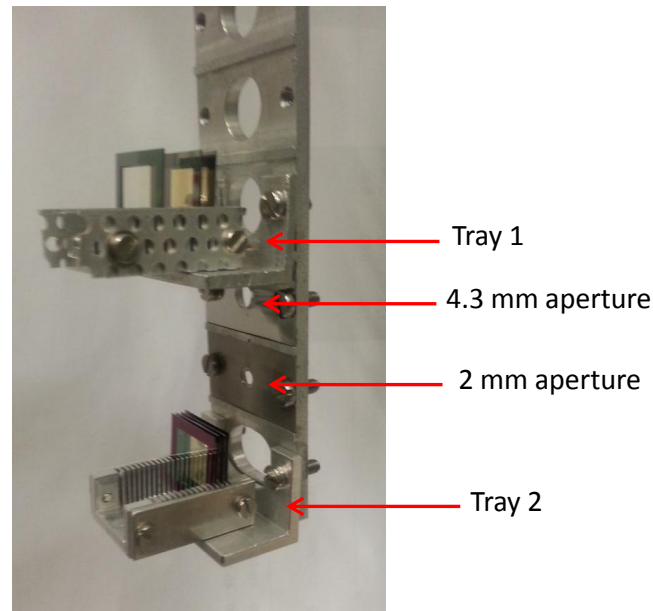


Figure 5.2. Photo of the ladder holder, on which the trays with SiN foils were mounted.

5.1.2. Settings

The magnetic rigidity of the analysing magnet (see Ch. 3.2.4.) was kept constant during the measurement sessions. As mentioned before, only a blank oxide sample was used, thus, the time of flight and energy of ^{93}Zr had to be interpolated from the ones from ^{92}Zr and ^{94}Zr . Keeping the magnetic rigidity constant allows the accurate comparison of the spectra of these two stable isotopes together with the isobar ^{93}Nb . In order to change the observed isotope the injector magnet field, the terminal voltage of the tandem and the voltage of the Wien filters were varied. For measurements with the stable isotopes additional attenuators were used. This was necessary because the current registered from the Faraday cup in front of the detector would result in too high count-rates in the detector itself. Count-rates over 1 kHz were avoided. The summing up of the dose could damage the semiconductor structure contributing to the worsening of the resolution or even yield a complete destruction of the detector.

Series of measurements were conducted with 0, 2, 3, 4 and 6 foils. The results with no foils were considered as references as they show the original energy and time spectrum without isobar separation. For each foil configuration incident ion energies between 70 MeV to 170 MeV were used. Expressed in units of MeV per nucleon the measurements were restricted to the region 0.8 MeV/amu to 1.8 MeV/amu. The voltage of the tandem accelerator was up to 12 MV and most of the practical results were obtained with voltages between 11.5 MeV and 10.7 MeV. Yet, the stripping yields in the accelerator of the considered isotopes were higher than 6% in all cases. The variety of combinations between initial energies and number of foils allowed us to scan a considerable part of the stopping power curves, Figure 4.3. In this way the optimal solution for isobar separation can be determined.

5.1.3. Results for $^{93}\text{Zr} - ^{93}\text{Nb}$ separation

After placing the foils in the trays and installing back the ladder holder in the beam-line, the exact position of the foils according to the beam had to be determined. For the measurement sessions with the passive absorber it was important that the ion beam path is adjusted along the axis of the beam line and passes centred through the SiN foils. In this way it was also assured that the ion beam will hit centrally the semiconductor detector. This adjustment was achieved with the help of the two apertures, placed on the ladder holder.

On the first place, the central position of the beam itself had to be determined. This was possible with the help of a quartz crystal, installed specially in the beam-line after the SiN holder position. For this purpose an ^{209}Bi ion beam was used, delivering high ion currents resulting in very distinctive spot on the crystal. Position adjustment was firstly performed with the aperture with diameter 4.3 mm and then, for high precision, with the one with diameter 2 mm.

In a previous work [20] the best separation was achieved with 8 SiN foils and energy of 168 MeV. An ionization chamber was used as a detector. The energies used for the current measurement were initially lower, that is why less foils were used in order to avoid fully stopping in the absorber. Additionally, this was also the conclusion from conducting the simulations with ^{87}Sr and ^{87}Rb .

The first measurement was started with two trays loaded with 2 and 6 foils respectively. In each measurement session the end energy and time of flight were recorded for the isotopes ^{92}Zr , ^{94}Zr and ^{93}Nb for 0, 2 and 6 foils at different initial ion energies. The ion current with a stable isotope was also recorded between the measurement sessions. A calibration of the detector at the beginning of the measurement session with the stable ions ^{92}Zr and ^{94}Zr was performed in order to obtain the energy in MeV and the time of flight in ns.

In Figure 5.4 plots from measurements with 0, 2 and 6 foils are presented for energy 90 MeV. On the x-axis the time of flight of the corresponding ion is plotted and on the y-axis the end energy, registered in the semiconductor detector.

It is important to notice that the presented spectra are actually superimposed plots from three consecutive measurements for the isotopes ^{92}Zr , ^{94}Zr and ^{93}Nb separately. In this way a clear picture could be obtained for the background for the searched ^{93}Zr . As expected, in Figure 5.3 a) it can be seen that for 0 foils the positions of ^{93}Zr and ^{93}Nb coincide and they cannot be separated as single isotopes. On the right, in green, is the position of ^{94}Zr , which has longer time of flight connected with lower energy. On the left, in red, is the registered spot of ^{92}Zr . It is faster with higher energy.

On Figure 5.3 b) can be seen that the separation between the isobars ^{93}Nb and ^{93}Zr is still not sufficient. The measurements with 6 foils showed that the scattering becomes too high and the background from the stable isotopes is too high.

Additionally, test higher and lower incident energies of the ions were conducted. The conclusion made was that with 2 foils the separation of the ^{93}Nb and ^{93}Zr peaks is not sufficient but with 6 foils the energy straggling becomes too high. Also, for higher energies better separation was observed than for lower ones.

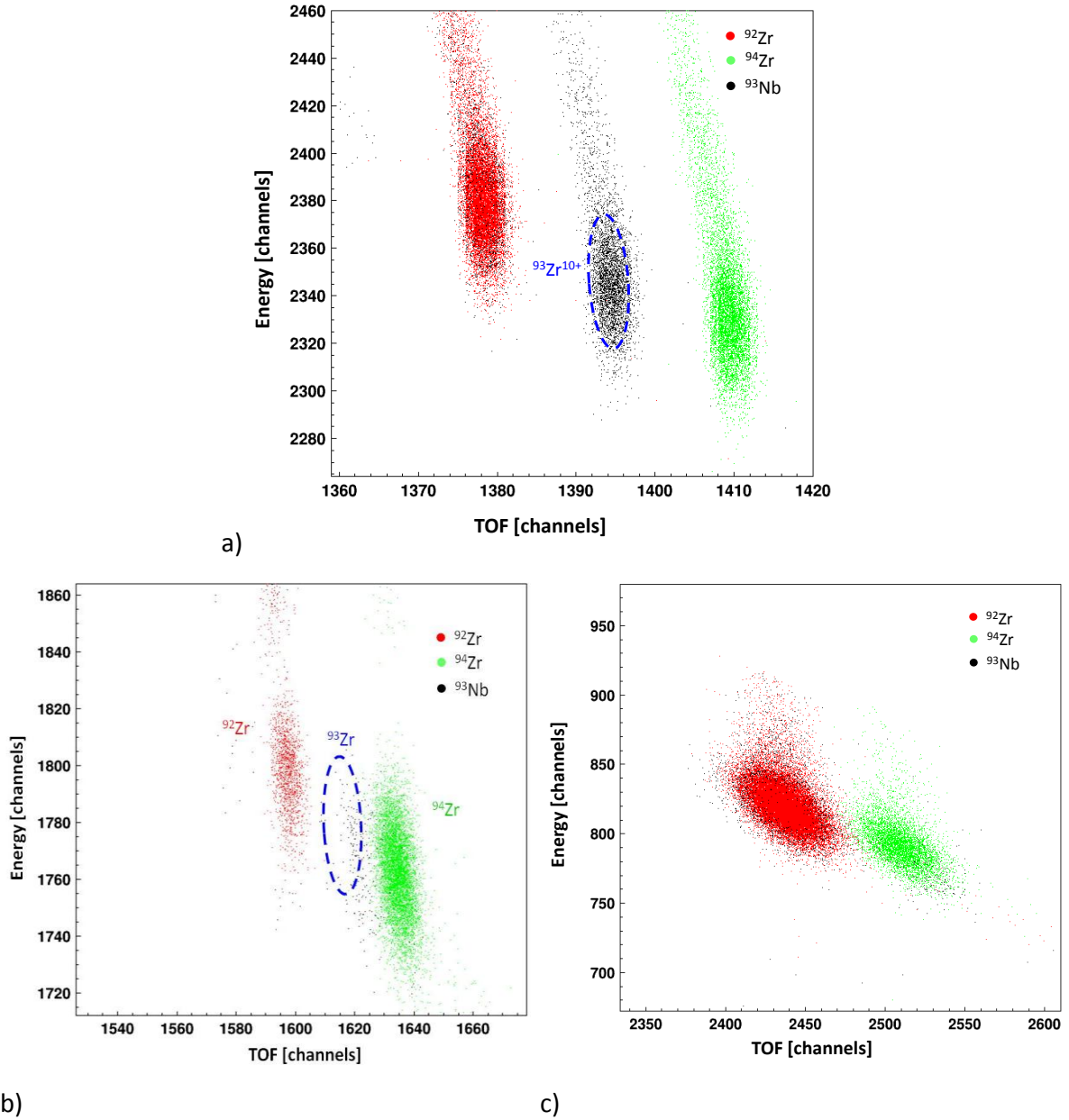


Figure 5.3. Superimposed spectra of ^{92}Zr , ^{94}Zr and ^{93}Nb for a) 0 foils, b) 2 foils and c) 6 foils at 90 MeV. The area in the blue ellipse marks the calculated position of ^{93}Zr with the corresponding peak width.

The next foil configuration tested was with 3 and 4 SiN foils. Ion energies of 140 MeV and 164 MeV were used. Because of technical problems, the third Wien filter was not used during these measurements. The results from the tests are presented on Figure 5.4.

Here again are shown the superimposed spectra from three different successive measurements for each foil configuration with ^{92}Zr , ^{94}Zr and ^{93}Nb . In the blue circle is the calculated position of the ^{93}Zr . Additionally, each superimposed plot was projected on the

time of flight x-axis. On the y-axis of the resulted plot are given the counts of the corresponding peak.

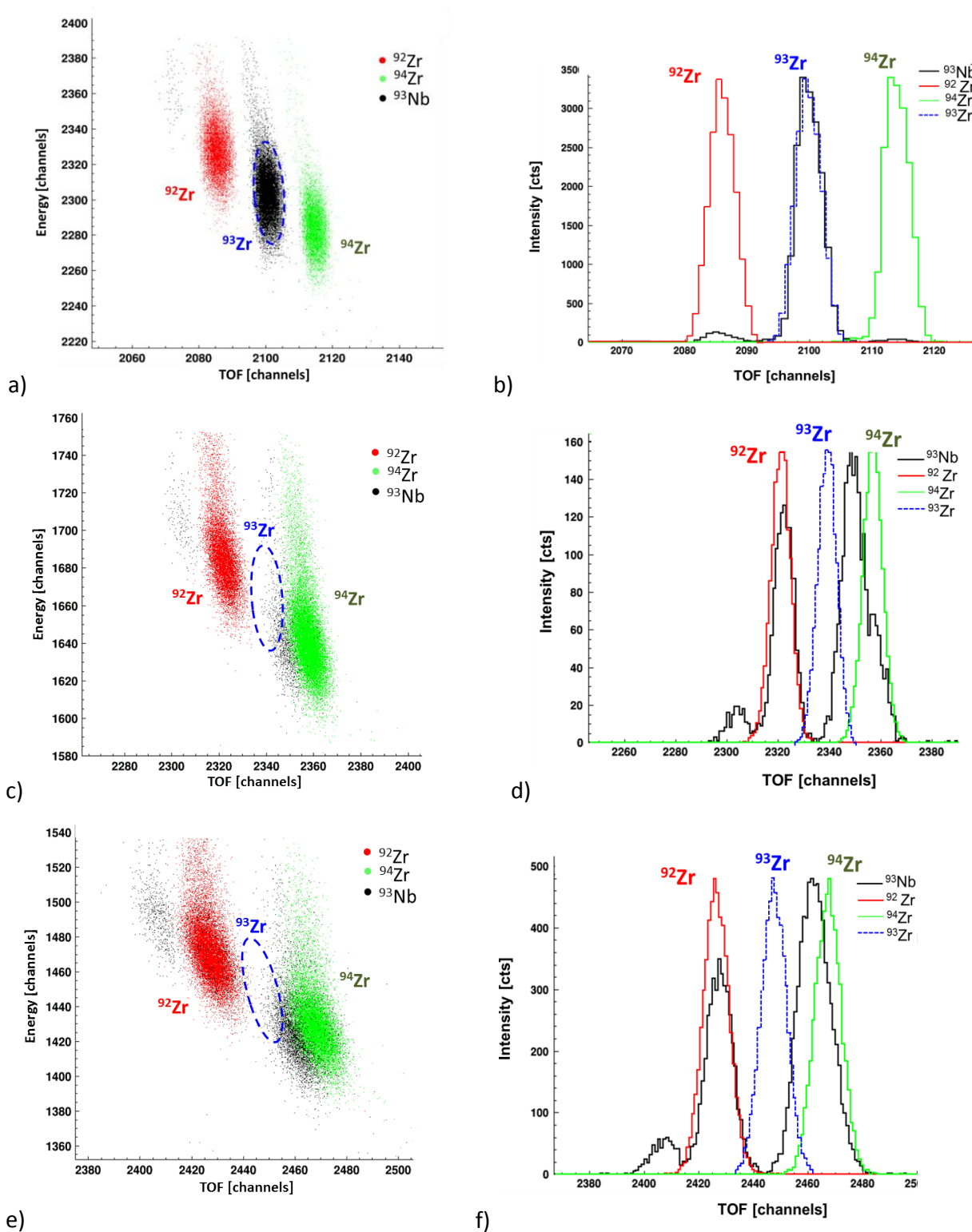


Figure 5.4. Superimposed spectra for ^{92}Zr , ^{94}Zr and ^{93}Nb for a) 0 foils, c) 3 foils and d) 4 foils at energy 14 MeV. For the plots on the right the superimposed plots were projected onto the time of flight x-axis for b) 0, d) 3 and f) 4 SiN foils.

This plot gave better information about the actual background occurring for mass 93. On Figure 5.4 b) can be seen that with no foils the area for ^{93}Zr and ^{93}Nb coincide completely, analogous to the previous measurement and expectations. There are some scattered events with mass 92 and 94, recognized as ^{92}Zr and ^{94}Zr , as the superimposed peaks from these two stable isotopes show. The difference in the ratio between the peak heights for these masses to the ^{93}Nb peak in the mass 93 spectrum result from ion optical effects due to different beam tuning.

Changing to 3 SiN foils gives already noticeable separation between ^{93}Zr and ^{93}Nb peaks, better distinguishable on Figure 5.4 c). The isobar ^{93}Nb loses more energy in the passive absorber than ^{93}Zr . Better separation was achieved with 4 SiN foils. The increased straggling due to the increased thickness of the absorber does not represent significant problem. It can be observed how the spot for ^{93}Nb moves towards the position of ^{94}Zr , away from the ^{93}Zr peak. With black is the spectrum obtained for mass 93 on Figure 4.4 b,d,f. It can be seen that some ions with mass 92 and 94 are registered. These are scattered events from foils and rest vacuum along the beam-line that manage to pass through all ion filters.

For calculation of the ^{93}Zr concentration in the sample, the counts of this isotope in the detector are needed. There is still an isotopic and isobaric background if the counts in the interpolated area are considered. That is why, analogously to the considerations and calculations in Chapter 3.4.2, a software cur was made. Based on this restriction, the concentration of the ^{93}Zr isotope in a sample could be determined. Still, as only blank samples were used for the measurements, no ^{93}Zr counts were expected and respectively no were found. That is why with the current results an upper detection limit for this isotope could be set. The results for 3 and 4 foils are summarised in Table 5.1.

Number of SiN foils	Energy [MeV]	T_{total} (%)	$C(^{93}\text{Zr})$
3	140	1.6	$1.9 \cdot 10^{-10}$
4	140	1.1	$1.7 \cdot 10^{-10}$
3	164	4.7	$1.9 \cdot 10^{-10}$
4	164	2.8	$1.2 \cdot 10^{-10}$

Table 5.1. Upper detection limit for ^{93}Zr . Information about the initial ion energy and the total transmission through the set-up is provided.

The results for 3 and 4 SiN foils show a similar upper detection limit for ^{93}Zr . Additionally, the value is lower than the previous limit of 10^{-9} [20]. It should be taken into account that the third Wien filter was not used during the measurement. Its utilization and optimization would further reduce the contribution of the mass 92 in the ^{93}Zr spectrum.

Considering the suppression between ^{93}Zr and ^{93}Nb , a Gauss approximation of the peaks was used. For this purpose the difference in the time of flight between the two peaks was measured. Also their standard deviation σ was recorded. On Figure 5.5 the calculation method used for suppression determination is presented, based on the readings for 4 foils SiN for 140 MeV.

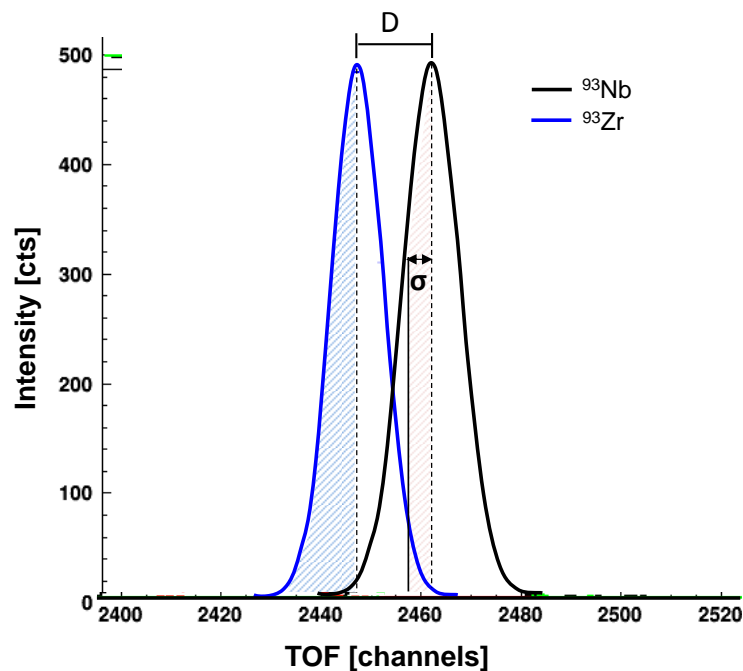


Figure 5.5. Practical example of the calculation of ^{93}Zr and ^{93}Nb separation. Plot, based on the measurements with 4 SiN foils at charge state 12+ (140 MeV). Description in the text.

The aim is to calculate the suppression of the unwanted ^{93}Nb . Only the region left from the maximum of the ^{93}Zr peak (blue) was considered. For this purpose the distance D between the peaks was calculated as a product of the standard deviation of the ^{93}Nb peak. Taking advantage of the embedded functions in the used calculation program, the ^{93}Nb counts left of the marked blue area were subtracted. This gives us as a result how many counts from the ^{93}Zr peaks can be accurately related to this isotope. Using this method, a suppression parameter for $^{93}\text{Zr}/^{93}\text{Nb}$ could be obtained and summarised in Table 5.2.

Number of foils	Separation $^{93}\text{Zr}/^{93}\text{Nb}$
0	1
3	1/80
4	1/360

Table 5.2. Separation $^{93}\text{Zr}/^{93}\text{Nb}$

From Figure 5.6 can be also seen that there is still a small contribution from ^{93}Nb in the examined area left from the ^{93}Zr peak. Compared to the absolute counts value, this contribution is very low. That is why it was not taken into account. However, there is significant contribution from the stable Zr isotopes, especially from ^{92}Zr (Figure 5.4).

Reducing the amount of ^{93}Nb in the sample itself would be an asset. Therefore, a scheme was developed to lower the isobar content using extraction chromatography with UTEVA resin and different reagent combinations. For this purpose dissolved metallic zirconium in Aqua Regia was used. The Aqua Regia was chosen as a substitute for the rather dangerous to handle HF. However, the dissolution of Zr was found to be rather slow process compared to previous trials with HF. High reaction temperatures were needed, $\sim 120^\circ\text{C}$, with short reaction times due to the fast passivation of the metallic zirconium. The chemical reduction of ^{93}Nb is an on-going project planned for future measurements.

5.1.4. Detector test

At the plots in Figures 6.4 and 6.5 one can notice the tails from the main peak towards higher energies and also to a lower time of flight. As this is not physically reasonable result the cause of these deviations was searched in the detector and/or electronics.

For comparison three detectors were tested. A PIPS detector with additional Al layer for better time resolution – TMPD 450-20-300 AM. Another PIPS detector without Al layer- PD 450-16-300 AM, was tested as well as a surface barrier detector AMETEK BF-028-400-60, used previously in the experiment. They were placed in a specially prepared set-up with an alpha ^{241}Am source. Registered from the detector, the alpha particles deliver single narrow energy peak. If the reason for the already mentioned high energy tails is the detector, also with this small experiment counts on the high energy side should be observed. Unfortunately, this test could not deliver an answer to the “tail” problem. All three detectors showed a sharp energy peak, caused by the alpha particles. Even the single events, detected with energies higher than the maximum peak, were too low in number to explain this artefact. Additionally, this test offered the opportunity to determine the energy resolution of the detectors. It was determined via the ratio FWHM/peak location, both measured as number of channels. The results for the resolution were similar for all three types:

Detector	Energy resolution [%]
TMPD 450-20-300 AM (Canberra)	1.2
PD 450-16-300 AM (Canberra)	1.1
AMETEK BF-028-400-60 (Oak Ridge)	1.3

Table 5.3. Energy resolution

The next examined possibility was the electronics. The three detectors were connected with a pulser, which delivers a signal with defined pulse height. The output signal was amplified from a pre- and afterwards a main amplifier and observed on an oscilloscope. Additionally, the signals were observed on a 2D plot with the measurement software (Marabou). It was noticed that the two PIPS detectors had differences in the amplified signal, which could explain the high energy artefacts on the Figure 5.3 and 5.4 plots. In comparison, the surface barrier detector showed clear signal. This is also supported from the fact that the latter detector has not shown distinctive high energy tails during its utilisation time.

The problem could not be conclusively located and eliminated. Still, it was concluded that the TMPD PIPS detector measurements can be still used because of the good time resolution. The high energy artefacts deliver some unwanted counts in the region of interest for measurements of ^{93}Zr . An attempt was made to keep the contribution of ^{92}Zr and ^{94}Zr as low as possible.

5.1.5. Cathode material

With the view of the optimising of the upper detection limit of ^{93}Zr the reduction of ^{93}Nb amount in the sample material was considered. For the tests conducted in this work ZrO_2 powder was mixed with Cu in order to increase the thermal and electrical conductivity of the cathode material (see Chapter 3.2.1). Copper do not produce negative ions in the mass range of ^{93}Zr but helps delivering higher Zr ion currents. The results showed considerable amount of ^{93}Nb in the detector, which affects the ^{93}Zr detection. A possibility to lower the detection limit is to lower the amount of ^{93}Nb in the sample. According to [59], mixing C, Cu or Ag with the ZrO_2 powder leads to contamination with Nb. This effect cannot be avoided even using high purity elements. That is why it was recommended to use only ZrO_2 as cathode material.

This assertion was tested with the TOF set up. Four different cathode materials were prepared and hammered into Cu holders. One sample contained ZrO_2 powder with no admixtures. For the other three, the powder was mixed with Cu, Au and C (in form of graphite) with ratio 1:1. Silver was not considered as an admixture due to the similar mass of ^{109}Ag to $^{93}\text{Zr}^{16}\text{O}^-$, extracted from the sample. The mixture with Cu was considered a reference. The comparison between the different variations of cathode material was done by comparing the detected ^{93}Nb , ^{92}Zr and ^{94}Zr counts per current per second in the detector. The final concentrations for each case were an average from a couple of consecutive measurements.

Sample material	$^{93}\text{Nb}/\text{nA}\cdot\text{s}$
ZrO_2	14
$\text{ZrO}_2 + \text{Cu}$	56
$\text{ZrO}_2 + \text{Au}$	29
$\text{ZrO}_2 + \text{C}$	24

Table 5.4. Counts ^{93}Nb per (current·seconds) for different cathode materials

The ZrO_2 mixed with Cu showed relatively high ^{93}Nb content. As mentioned before (see Chapter 5.1.3), ^{93}Nb can be successfully suppressed in the calculations. The difficulty is the background originating from the stable ^{92}Zr and ^{94}Zr . That is why the ZrO_2 mixture with Cu was considered for a good choice.

5.1.6. ^{99}Tc and ^{99}Rb

Additional measurement was performed for the isobars ^{99}Tc and ^{99}Rb . The purpose was to experimentally check if the discussed method in this work is applicable for other isobar pairs. ^{99}Tc is an important isotope in the nuclear waste disposal problem, because of its high fission production yield, very long half-life ($T_{1/2} = 2.1 \cdot 10^5 \text{ a}$) and high mobility in the environment. ^{99}Tc is traceable in higher concentration with methods such as ICP-MS or radiometric counting. However, to go below the limits of these two methods AMS is the method of choice. Challenges present the interfering isobar ^{99}Ru . The suppression of ^{99}Ru in the ^{99}Tc measurements was evaluated for 3 and 4 SiN foils. The results are summarised in Table 5.5. The contribution from the tails to higher energies and lower TOF are not taken into account.

Number of foils	Separation $^{99}\text{Tc}/^{99}\text{Ru}$
0	1
3	$1/(9 \cdot 10^3)$
4	$1/(1.7 \cdot 10^5)$

Table 5.5. Suppression of ^{99}Ru during ^{99}Tc measurements

The tests with this higher mass showed better suppression than with mass 93 (Table 5.5). This is interesting result, probably caused by the lack of stable neighbouring isotopes.

5.1.7. Comparison between test and SRIM simulation for ^{92}Zr and ^{94}Zr

Simulations with ^{92}Zr and ^{94}Zr for different absorber thickness were made. These two isotopes are stable and well-studied. Also, they are direct neighbours of ^{93}Zr and, as already mentioned, information about the behaviour of ^{93}Zr in the passive absorber can be obtained by interpolation. That is why it was interesting to check how far the experimental results follow the predictions from the SRIM simulations. During measurements the end energies and time of flight of ^{92}Zr and ^{94}Zr were already measured for different number of SiN foil configurations. The energy loss and TOF were compared to the corresponding quantities from SRIM. The results for ^{94}Zr with 2 foils SiN are presented on Figure 5.6. The results for ^{92}Zr showed the same behaviour and are not explicitly presented.

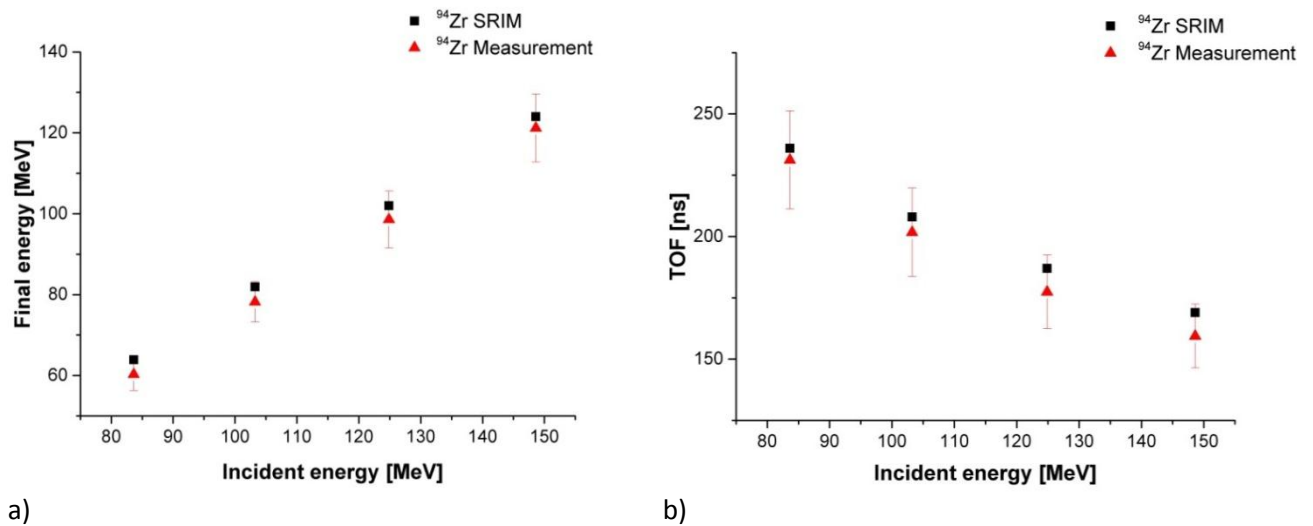


Figure 5.6. Comparison between SRIM simulations and measurement results for a) final ion energy and b) TOF for ^{94}Zr with 2 foils at different incident ion energies.

The error bars represent the error due to the ion current fluctuations, measured on the last Faraday cup in front of the detector, and the energy straggling, causing a Gauss distribution of the energy loss peak. The results on Figure 5.6 are in good agreement with the SRIM simulation. If the simulations and the measurements with 6 SiN foils are compared high deviations from the stopping power curve simulations are observed. The reason is that the foils represent 6 μm thick absorber. This corresponds to a very thick target case (see Chapter 4.1.2). In this instance special calculations should be made in addition to the simulation.

5.2. GAMS beam line

In addition to the measurements with the Time-Of-Flight beam line using a passive absorber, tests were conducted with the GAMS. The use of a gas filled magnet is an established method for isobar separation (work method described in Chapter 3.3.1). Previous works point out the advantages of this measurement method [20] [35]. An example is the measurement with ^{93}Mo for which an upper detection limit $^{93}\text{Mo}/^{92}\text{Mo}$ smaller than 10^{-9} was achieved [60]. ^{93}Mo is an interesting isotope also in our case because of the very similar background situation to ^{93}Zr . Measurements prior to this thesis [20] have shown that analogously to ^{93}Mo , GAMS is a promising method for isobaric separation of ^{93}Zr and ^{93}Nb . The upper detection limit reached is in the order of 10^{-7} . The goal of the described measurements was to lower, if possible, the detection limit by testing different combinations of magnet field strength, magnet and ionisation chamber pressures.

If the considerations in Chapter 3.3.1 are followed, ^{93}Zr and ^{93}Nb should have different radius of the curvature due to the passage through the N_2 gas in the gas-filled magnet (GFM). This is also made clear with the Sayer formula and the corresponding plot in Figure 3.5. If the magnetic field B is taken constant, which is also the case, ^{93}Nb shows lower rigidity and thus smaller radius in the GFM. If a suitable magnetic field is chosen, then the ^{93}Nb distribution on the output window of the GFM can be cut out with the help of two slits.

The pressure in the magnetic chamber can be varied which leads to gas density changes. The ions of the two isobars undergo collisions with the gas and develop an averaged charge state \bar{q} . The ionisation chamber is filled with isobutane gas (C_4H_{10}), which pressure can be also varied, independently from the pressure in the GFM. For a constant gas pressure the stopping in the detector is determined from the average charge state of the ions. For partially stripped ions the stopping power can be approximated to be

$$\frac{dE}{dx} \propto \bar{q}^2 \quad (5.1)$$

Increasing the pressure in the detector chamber the isobutane the distance between molecules is reduced which leads to shorter free path length of the ^{93}Zr and ^{93}Nb ions. The energy loss is higher and they are stopped earlier in the ion chamber. The positioning of the anodes in the detector (Chapter 3.3.1) gives the opportunity to follow the energy deposition in depth and the spatial distribution of the incoming ions. An important point is to vary the pressure in the ion chamber in accordance to the pressure in the GFM and hence obtain well separated signals from the two examined isobars on the different electrodes. This should be achieved together with the use of well selected magnetic field in the GFM chamber, which contributes to the maximal separation of the isobaric background of ^{93}Zr . The contribution of all three parameters was investigated for incident ions with energy of 164 MeV. The sample used was a blank Zr sample. That is why the position of ^{93}Zr had to be averaged from the positions of ^{92}Zr and ^{94}Zr .

A practical way to separate only the mass of interest for further calculations was to use the time of flight measurement set-up in front of the GAMS. It is realised via two multichannel plate detectors, placed in the beam line before the gas-filled magnet. The spectrum obtained is shown in Figure 5.7.

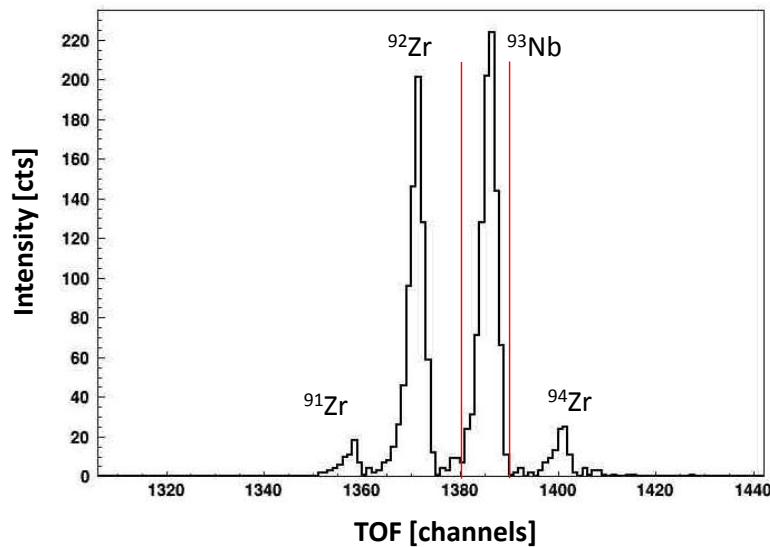


Figure 5.7. TOF spectrum of mass 93 for ion energy 140 MeV.

On the TOF spectrum can be seen not only the peak for mass 93 but also peaks for the stable masses 91, 92 and 94. In order to investigate the separation of ^{93}Zr from ^{93}Nb in the gas chamber detector it is reasonable to exclude all other masses. This is achieved by setting a software “window”, which defines only the region of interest. In Figure 5.7 the window is indicated with red lines at the example of mass 93. Analogously, windows were set for mass 92 and 94, representing ^{92}Zr and ^{94}Zr , in order to obtain estimated data for the behaviour of ^{93}Zr .

5.2.1. Pressure investigation

After assuring that only the mass of interest is considered, different magnetic field-pressure configurations were investigated. The purpose was to optimise the separation between ^{93}Zr and ^{93}Nb and to lower the detection limit for ^{93}Zr . In the first place, the magnetic field was kept constant on $B = 960$ mT. Three different combinations between pressure in the ion chamber, P_{IC} , and pressure in the magnet chamber, P_{GFM} , were tested. The signals from the two first electrodes from the detector give additionally to the deposited energy reading also position information. This was used to observe the position of the mass 93 peak for different P_{GFM} values. A superimposed plot is presented on Figure 5.8 where the position of the peaks is plotted for different pressure configurations.

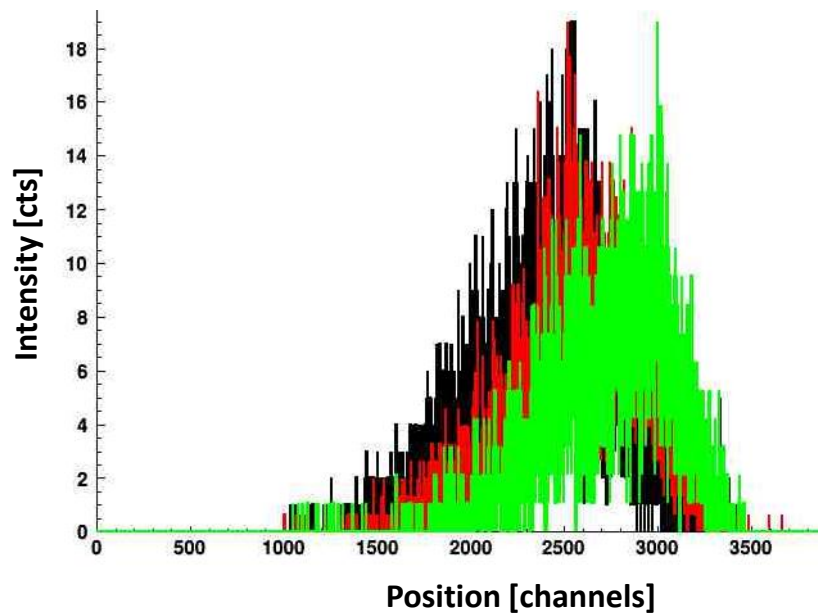


Figure 5.8. Superimposed spectrum, showing the position of mass 93 peak for $P_{\text{IC}} = 40$ mbar and $P_{\text{GFM}} = 4.2$ mbar (black), $P_{\text{IC}} = 37$ mbar and $P_{\text{GFM}} = 4.6$ mbar (red) and $P_{\text{IC}} = 34$ mbar and $P_{\text{GFM}} = 5$ mbar (green).

The observed results show that with increase of the P_{GFM} the flying path radius for both ^{93}Zr and ^{93}Nb , mass 93, decreases (shifts to the right). The stopping power for the two isobars in the GFM will be slightly different. These effects, together with adjustment of the slits at the exit of the GFM, can be used to create a window in the position readings and thus exclude part of the interfering ^{93}Nb ions.

Taking into account the change of the detector pressure, the behaviour of the ions of mass 93 can be also investigated. According to the considerations, with increase of the gas pressure the incident ions should be stopped earlier in the detector. As the ^{93}Zr and ^{93}Nb have

different stopping power in the isobutane gas, their ΔE signals will be slightly different. Accordingly setting windows on each of the detector signals contributes to the ^{93}Nb suppression and the detection limit could be reduced.

On Figure 5.9 are presented the results from the energy readings of the first electrode, E1. The shifting of the energy signal towards lower values with increasing pressure can be observed due to the increased energy before the first electrode. This leads to lowering the end energy and higher energy difference. This effect is supported by the detail that the energy of the incident ions per mass unit is 1.7 MeV/amu and thus higher than those of the Bragg peak ~ 0.8 MeV/amu calculated from Nortcliffe and Schilling tables. According to this, reducing the energy due to the increased stopping power leads to higher energy losses.

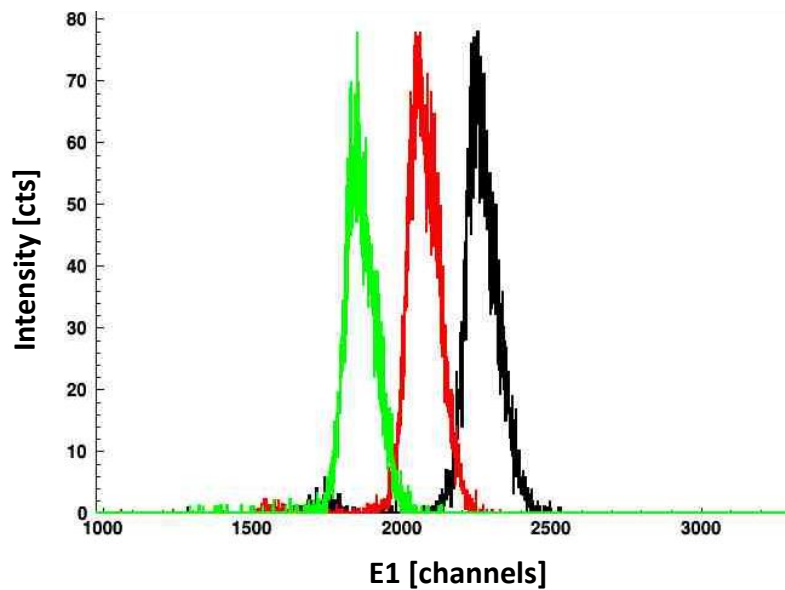


Figure 5.9. Superimposed spectrum, showing the E1 energy reading of mass 93 peak for $P_{IC} = 40$ mbar and $P_{GFM} = 4.2$ mbar (black), $P_{IC} = 37$ mbar and $P_{GFM} = 4.6$ mbar (red) and $P_{IC} = 34$ mbar and $P_{GFM} = 5$ mbar (green).

In view of the position of ^{93}Nb and the interpolated position of ^{93}Zr from the measurements of ^{92}Zr and ^{94}Zr , the separation between the two isobars could be determined. The model for the calculations is already presented on Figure 4.2. The difference between the positions of the two peak maxima was calculated and correlated to the measured FWHM of the ^{93}Nb peak. Both values exhibit uncertainties, which originate from the deviations between the Gauss approximation of the readings and the real peaks. The error bars on the plot are calculated from the linear addition of the separate uncertainties.

A tendency is observed – with increasing pressure P_{GFM} and respectively decreasing P_{IC} the separation between the ^{93}Zr and ^{93}Nb peaks is lowered. This leads to the conclusion that among the investigated pressure combinations with constant magnetic field, the set with

$P_{IC} = 40$ mbar and $P_{GFM} = 4.2$ mbar delivers the best results. Thus, this pressure configuration was selected for the next measurements with variable field in the magnet.

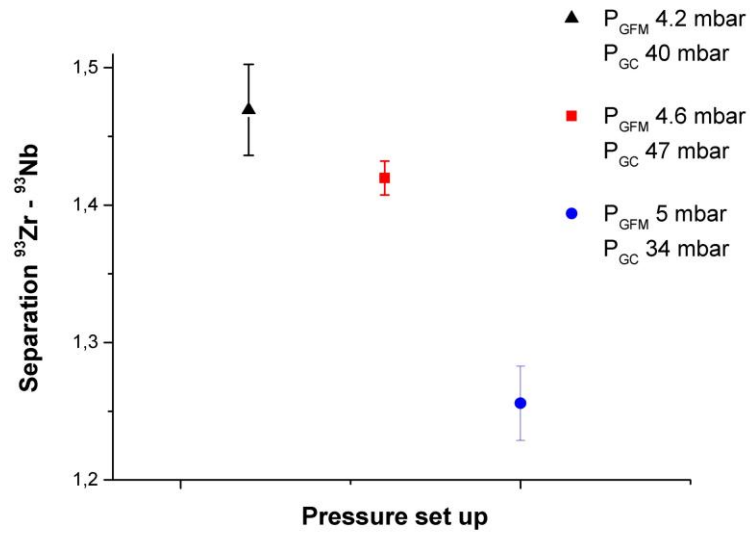


Figure 5.10. Separation between ^{93}Zr and ^{93}Nb for different pressure combinations for ion energy 140 MeV in the position measurement after GFM.

The subsequent tests were performed with constant pressure in GFM and ion chamber. The magnetic field in the GAMS was varied between 960 mT and 1017 mT. The position of the mass 93 peak, representing ^{93}Nb in the case of the blank sample, was evaluated for seven fields in total: 960, 969, 976.39, 978, 986, 995 and 1017 mT. An original measurement is presented on Figure 5.11. With the purpose of clarity, this is a superimposed plot for only three selected field strengths.

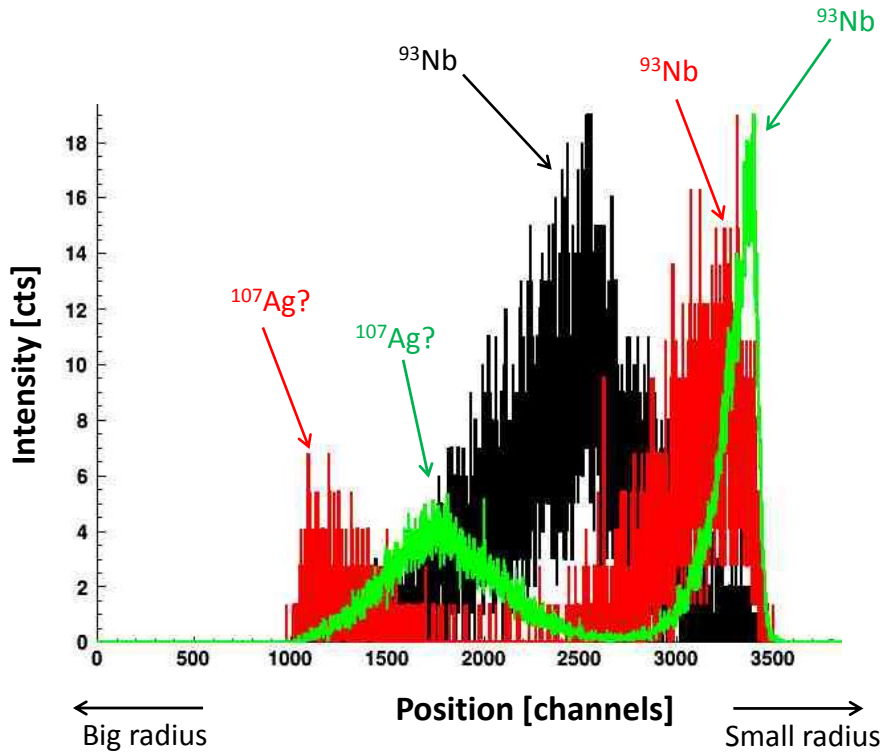


Figure 5.11. Superimposed spectrum, showing the position reading of mass 93 peak for $B = 960$ mT (black), $B = 978$ mT (red) and $B = 995$ mT (green).

The tendency for peak shift to the lower curvature radii with increasing magnetic field, caused by the increasing Lorentz force, is visible. This is the reason why the peaks for fields over 978 mT are cut out from the slits after the GFM. Unfortunately, the differences in the rigidity for ^{93}Zr and ^{93}Nb are quite small and the two peaks overlap. That is why a full suppression of the isobar interference will not be realistic.

For this field range an interesting artefact is also noticed. Another peak is visible in the region with bigger radius of curvature as the one of mass 93. This means that ions with another mass pass through the slits and enter the ion chamber. Unfortunately, these additional counts cannot be neglected while measuring mass 93, because of the high count rate they deliver in the detector. This additional ion species should have the same mass-to-charge state ratio as the ions of interest. Based on the noticed bigger radius the conclusion can be made that the mass of the searched ions should be also bigger. In our case, for mass 93 and charge state 13+, possible candidate is $^{107}\text{Ag}^{15+}$ with $m/q \sim 7.1$. All used blank samples were prepared with ZrO_2 mixed with Cu and hammered into Cu holders. However, during previous measurements for other projects some samples hammered in Ag holders were used. There were also cases when the sample material was mixed with Ag. In this way a so called “cross-talk” occurred and some of the silver ions could still be found in the ion source. The contribution from the ^{107}Ag can be avoided by using a window on the time-of-flight signal. Still, the magnet field was chosen to be lower than 978 mT, where these artefacts were firstly

noticed. For further considerations the magnetic field in the GAMS was set to 960 mT, where ^{93}Nb is centred. No position separation with the slits after the GFM was used.

5.2.2. Detection limit of ^{93}Zr

The two peaks for ^{93}Zr and ^{93}Nb are overlapping in the position as well as in energy readings. Therefore, it is not meaningful to cut completely with windows the ^{93}Nb peak because the most of the ^{93}Zr peak will be also cut. The aim was to combine the windows in the different readings in such a way, as to obtain maximum ^{93}Zr counts with insignificant amount of ^{93}Nb interference. Figure 5.5 represents the considerations for the TOF beam line but can be used also here for illustration.

In order to calculate the detection limit for ^{93}Zr the transmission of the system is needed. It can be separated again into physical and software transmission.

The physical transmission was determined as the ratio between the count rate in the detector and the count rate in the Faraday cup in from of the GAMS set-up for a stable Zr isotope and results in

$$T_{phys} = \frac{R_{det}}{R_{cup}} = \frac{(events/t) \cdot Attenuator}{\bar{I}_{92Zr} / (q \cdot e)} \quad (5.2)$$

In this equation q is the charge state of the ions, e is the elementary charge and \bar{I} is the averaged current reading from the Faraday cup. The use of an attenuator should be also taken into account. The physical transmission was averaged over several measurements and was determined to be 23.15%.

The software transmission was calculated separately for each combination of windows for the different signals. It also shows the losses introduced by applying a window and follows the formula

$$T_{soft} = \frac{events\ with\ windows}{events\ without\ windows} \quad (5.3)$$

The concentration of ^{93}Zr to the background was obtained with Equations (3.14) and (3.15). Analogously to the considerations with the TOF beam line, the obtained value can be considered as an upper detection limit because of the blank sample used.

A starting point for calculation of the $^{93}\text{Zr}/\text{Zr}$ ratio was the determination of initial conditions. These included symmetrical cuts with width 2σ on all energy readings from the detector – E_t , E_1 , E_2 , E_3 , E_4 and E_5 (Figure 3.6). No cut was applied on the TOF signal. In Table 5.6 are presented the results for detection limits together with the cuts used in addition to the initial symmetrical ones. The corresponding transmissions are also included.

T_{phys} [%]	T_{soft} [%]	$^{93}\text{Zr}/\text{Zr}$	Nº of additional cuts	Signal cut type
23.15	51.35	$1.73 \cdot 10^{-8}$	0	initial
23.15	26.55	$8.19 \cdot 10^{-9}$	1	+ TOF
23.15	21.93	$2.45 \cdot 10^{-9}$	2	+ TOF and asymmetrical of position
23.15	20.17	$1 \cdot 10^{-9}$	3	+ TOF, asymmetrical of position and E5
23.15	19.03	$4.7 \cdot 10^{-10}$	4	+ TOF, asymmetrical of position, E5 and E4

Table 5.6. Upper detection limit for ^{93}Zr with the physical and software transmission of the system

The lowest detection limit was $4.7 \cdot 10^{-10}$, applying 4 windows in the time of flight, position and in the E4 and E5 energy signals from the detector. This result is in the same order of magnitude as the one with the Time-of-Flight beam line. It was achieved with an acceptable signal loss, $T_{\text{soft}} \sim 20\%$. Such a comparison can be made because of the same way the transmission of the system was determined – using a blank sample.

Summary and outlook

Within the scope of this master thesis the detection of long-lived radionuclides on the example of ^{93}Zr was investigated. The background situation resulting from a stable isobar and two neighbouring stable isotopes made the detection of this isotope challenging. That is why two different detection methods were utilized. Using a passive absorber proved to be an effective method for isobar separation. Prior simulations and tables calculations for the behaviour of ^{93}Zr and ^{93}Nb in the absorber material delivered controversial results and thus leading to a direct experimental approach. With the measurements conducted we were able to determine an absorber thickness for which, with the available ion energies from the tandem accelerator, the current detection limit of $1.7 \cdot 10^{-10}$ could be achieved. The tests performed with the GAMS beam line showed that the method with a gas-filled magnet also proved to be promising considering ^{93}Zr and ^{93}Nb isobar separation. Using in addition the time of flight set up on this beam line, a better mass separation was achieved. The upper detection limit of $4.7 \cdot 10^{-10}$ was obtained.

The results show that for the first time ultra trace amounts of a long-lived radioisotope can be measured. Future plans are focused on improving the detection limit. The final ion energies were adjusted according to the current limitations of the tandem accelerator. Using higher energies and respectively modifying the absorber thickness could improve the detection limit. Turning on and optimising the third Wien filter also will contribute to the isotopic suppression. Reducing the amount of ^{93}Nb in the sample itself would be an asset..

Using a standard sample is also an asset in order to verify the transmissions and the detection limits. A sample with defined ^{93}Zr amount will help for reduction of the detection limit for the GAMS. There was a standard Zr plate available in metallic form, already irradiated in the reactor. It was necessary to dissolve the material and then to oxidise it so as to obtain ZrO_2 powder. The application of a standard sample is also a subject of future measurements.

Bibliography

- [1] J. Emsley, *Nature's Building Blocks: An A-Z Guide to the Elements*, New York: Oxford University Press Inc., 2011.
- [2] J. Peterson, „Radiological and Chemical Fact Sheets to Support Health Risk Analyses for Contaminated Areas,“ Argonne National Laboratory, Environmental Science Division, U.S. Department of Energy, 2007.
- [3] L. C. Beck, *A condensed view of the present state of the science, with copious references to more extensive treatises, original papers*, E.W. & C. Skinner.
- [4] Intersectinsight, „Zirconium sponge plant launched in China,“ 12 6 2012. [Online]. Available: intersectinsight.com. [Accessed 03 2015].
- [5] W. Espe, *Zirkonium – Seine Herstellung, Eigenschaften und Anwendungen in der Vakuumtechnik*, Füssen/Bayern: C.F. Winter'sche Verlagshandlung, 1953.
- [6] D. Lee et al, „Zirconium: biomedical and nephrological applications,“ Bd. 56(6), pp. 550-6, 2010 Nov-Dec.
- [7] G. S. Brady, H. R. Clauser und J. A. Vaccari, „Materials Handbook 15th ed.,“ McGraw-Hill Professional., 2011, p. 1063–.
- [8] R. Krishnan und M. Asundi, „Zirconium alloys in nuclear technology,“ *Proc. Indian Acad. Sci.*, Bd. 4, pp. 41-56, April 1981.
- [9] F. Erbacher und S. Leistikow, *A Review of Zircaloy Fuel Cladding Behaviour in a Loss-of-Coolant Accident*, Kernforschungszentrum Karlsruhe GmbH, September 1985.
- [10] P. Cassette et al, „Determination of ^{93}Zr decay scheme and half-life,“ *Applied Radiation and Isotopes*, Bd. 68, pp. 122-130, 2010.
- [11] A. Nystrom und M. Thoennessen, „Discovery of Yttrium, Zirconium, Niobium, Technetium, and Ruthenium Isotopes,“ Preprint submitted to Atomic Data and Nuclear Data Tables, November 13, 2010.
- [12] „Nuclear Data Center,“ Japanese Atomic Energy Agency, 02 12 2013. [Online]. Available: <http://www.ndc.jaea.go.jp/nucldata/>. [Zugriff am 23 04 2015].
- [13] „Physics of Uranium and Nuclear Energy,“ World Nuclear Association, Updated September 2014. [Online]. Available: <http://www.world-nuclear.org/info/Nuclear-Fuel-Cycle/Introduction/Physics-of-Nuclear-Energy/>. [Accessed 30 04 2015].

- [14] „Nuclear Reactors, Neutron Propagation,“ Laboratory for Reactor Physics and Systems Behaviour, Ecole Polytechnique Federale de Lausanne, 2010.
- [15] S. Popov et al, „Thermophysical Properties of MOX and UO₂ Fuels Including the Effects of Irradiation,“ UT-Battelle, LLC, Oak Ridge, November 2010.
- [16] „Tables of Physical & Chemical Constants 4.7.2 Neutron cross-sections,“ Kaye & Laby Online, Version 1.0 2005 (16th edition 1995).
- [17] M. Herod, „What should we do with radioactive waste?,“ Blogs of the European Geosciences Union, 2015.
- [18] J. Kopecky, „Atlas of Neutron Capture Cross Sections,“ International Atomic Energy Agency, Vienna, 1997.
- [19] IAEA, „Using Isotopes to Understand the Oceans and Climate Change,“ in *IAEA General Conference*, Vienna, 2007.
- [20] K. Hain, „Accelerator Mass Spectrometry Relevant for Nuclear Waste Transmutation,“ Technische Universität München, Munich, 2011.
- [21] J. Plant, P. Simpson, B. Smith und B. Windley, „Uranium ore deposits: products of the radioactive earth,“ *Reviews in Mineralogy and Geochemistry*, Bd. 38, pp. 255-319, 1999.
- [22] A. Bonardi, „Study of Cosmic Ray Neutrons,“ Università degli Studi di Torino, Torino, 2010.
- [23] A. Gurevich und V. Antonova, „Strong Flux of Low-Energy Neutrons Produced by Thunderstorms,“ *Physical Review Letters (American Physical Society)*, Bd. 12, Nr. 108, 2012.
- [24] B. M. Kuzhevskij, O. Y. Nechaev und A. Sigaeva, „Distribution of neutrons near the Earth's surface,“ *Natural Hazards and Earth System Sciences*, Bd. 3, p. 255–262, 2003.
- [25] G. V. Gorshkov, V. A. Zyabkin und O. S. Tsvetkov, „The neutron background at the surface of the earth,“ *Soviet Atomic Energy*, Bd. 17, Nr. 6, pp. 1256-1260, December 1964.
- [26] K. Komura et al, „Variation of Environmental Neutron Flux with the Depth of Water and Soil,“ *Journal of Nuclear and Radiochemical Sciences*, Bd. 9, Nr. 2, pp. 45-47, 2008.
- [27] N. Hoffman und D. Holden, „Spontaneous fission half-lives for ground-state nuclides,“ *Pure Appl. Chem.*, Bd. 72, Nr. 8, p. 1525–1562, 2000.
- [28] M. Lugaro und G. Tagliente, „The impact of updated Zr neutron-capture cross sections and new asymptotic giant branch models on our understanding of the s process and the origin of stardust,“ Argonne National Laboratory, Argonne, 2013.

- [29] I. Dillmann, R. Plag, F. Käppeler und T. Rauscher, „Karlsruhe Astrophysical Database of Nucleosynthesis in Stars,“ 2013.
- [30] R. Runkle, „Opportunities for Decay Counting of Environmental Radioisotopes Using Ultra-low-background Detection Systems,“ Pacific Northwest National Laboratory, Richland, Washington, 2012.
- [31] T. Oliveira et al, „Radiochemical methodologies applied to determination of zirconium isotopes in low-level waste samples from nuclear power plants,“ *J Radioanal Nucl Chem*, Bd. 302, pp. 41-47, 2014.
- [32] R. E. Wolf, „What is ICP-MS?,“ U.S. Geological Survey, March 2005.
- [33] M. Bertaux et al, „Analytical Improvements For Long-Lived Radionuclides Determination In Zircaloy Hulls,“ in *Nuclear Fuel Cycles for a Sustainable Future*, Montpellier, 2008.
- [34] R. Middleton, „A versatile high intensity negative ion source,“ *Nuclear Instruments and Methods*, Nr. 214, pp. 139-150, 1983.
- [35] K. Knie, Beschleunigermassenspektrometrie mit Isobarenspeparation in einem dediziertem gasgefüllten Magneten, Munich: Technische Universität München, 1996.
- [36] N. Bohr, „On the theory of the decrease of velocity of moving electrified particles through matter,“ *Phys. Mag. Series 6*, Bd. 145, Nr. 25, 1913.
- [37] N. Bohr, „On the decrease of velocity of swiftly moving electrified particles in passing through matter,“ *Phys. Mag. Series 6*, Bd. 178, Nr. 30, 1915.
- [38] M. Tufan, „Stopping Power Calculations for Partially Stripped Projectiles in High Energy Region,“ *ACTA PHYSICA POLONICA A*, Bd. 107, Nr. 3, pp. 459-472, 2005.
- [39] R. Sayer, „Semi-empirical formulas for heavy-ion stripping data,“ *REVUE DE PHYSIQUE APPLIQUÉE*, Bd. 12, pp. 1543-1546, 1977.
- [40] P. Ludwig, „Search for Superheavy Elements in Nature with Accelerator Mass Spectrometry,“ Master's thesis, TUM, Munich, 2010.
- [41] Canberra, „Passivated Implanted Planar Silicon (PIPS®) Detectors,“ Application note.
- [42] S. H. Connell und R. Tegen, *Fundamental and Applied Aspects of Modern Physics*, World Scientific Publishing Co. Pte. Ltd, 2001.
- [43] C. Race et al, „The treatment of electronic excitations in atomistic models of radiation damage in metals,“ *Reports on Progress in Physics*, Bd. 73, Nr. 11, 2010.

- [44] P. Sigmund, *Stopping of Heavy Ions: A Theoretical Approach*, Springer, 2004.
- [45] J. Lindhard, M. Scharff und H. E. Schiott, „Range concepts and heavy ion ranges (Notes on atomic collisions, II),“ *Kgl. Danske Videnskab. Selskab. Mat. Fys. Medd.*, Bd. 33, Nr. 14, pp. 1-49, 1963.
- [46] O. Firsov, „Interaction energy of atoms for small nuclear separations,“ *Zh. Eksp. Teor. Fiz.*, Bd. 32, pp. 1464-1469, 1957.
- [47] L. Northcliffe und R. Schilling, „Range and Stopping - Power Tables for Heavy Ions,“ *Nuclear Data Tables*, Bd. 7, pp. 233-463, 1970.
- [48] H. Bethe und J. Ashkin, „Passage of Radiation through Matter,“ in *Experimental Nuclear Physics Vol 1*, ed. E. Segre, John Wiley & Sons, Inc., 1953, pp. 166-358.
- [49] P. Sigmund, *Particle Penetration and Radiation Effects: General Aspects and Stopping of Swift Point Charges*, Springer, 2006.
- [50] M. Kumakhov und F. Komarov, *Energy Loss and Ion Ranges in Solids*, Gordon and Breach Science Publishers, 1981.
- [51] J. F. Ziegler, J. P. Biersack und M. D. Ziegler, *SRIM - The Stopping and Range of Ions in Matter*, SRIM Company, 2008.
- [52] V. Meshakin, „Energy loss straggling of fast heavy ions with account of the spatial correlation effect,“ *J. Phys. B: At. Mol. Opt. Phys.*, Bd. 33, pp. 709-715, 2000.
- [53] F. Besenbacher et al, *Straggling in Energy Loss of Swift Hydrogen and Helium Ions in Gases*, Copenhagen: Vol. 40. Kommissionær, Munksgaard, 1981.
- [54] S. Ouichaoui et al, „Energy loss straggling of swift heavy ions in metal foils at $E/A \sim 2$ MeV/u,“ *Nuclear Instruments and Methods in Physics Research Section B: Beam Interactions with Materials and Atoms*, Bd. 164, pp. 259-267, 2000.
- [55] W. Chu, „Calculation of energy straggling for protons and helium ions,“ *Physical Review A*, Bd. 13, Nr. 6, p. 2957, 1976.
- [56] Q. Yang und D. O'Connor, „Empirical formulae for energy loss straggling of ions in matter,“ *Nuclear Instruments and Methods in Physics Research B*, Bd. 61, pp. 149-155, 1991.
- [57] Silson, Silson Ltd, [Online]. Available: <http://www.silson.com/>. [Zugriff am 31.5.2015].
- [58] „Personal communication with Malcolm Cox, Silson Ltd,“ from January 2015.
- [59] W. Lu et al, „Zr/Nb isobar separation experiment for future ^{93}Zr AMS measurement,“

Nuclear Instruments and Methods in Physics Research Section B: Beam Interactions with Materials and Atoms, 2015.

- [60] G. Rugel et al, „Measurement of the Activation Product ^{93}Mo via AMS. Technical report,“ Maier-Leibnitz-Laboratory, Garching, München, 2007.
- [61] J. K. Shultis und R. E. Faw, *Fundamentals of nuclear Science and Engineering*, Marcel Dekker Inc., 2002.